2023-04-12

Role of dual breakwaters and trenches on efficiency of an oscillating water column

Naik, N

10.1063/5.0146004
Physics of Fluids
AIP Publishing

Title:
Role of dual breakwaters and trenches on efficiency of an oscillating water column

Journal:
Physics of Fluids

Author names and affiliations:
Nikita Naik[a], Siming Zheng[b,c], Harekrushna Behera[a,d,*]

a Department of Mathematics, SRM Institute of Science and Technology, Kattankulathur, Tamil Nadu, India
b School of Engineering, Computing and Mathematics, University of Plymouth, Drake Circus, Plymouth, PL4 8AA, United Kingdom
c State Key Laboratory of Hydraulic Engineering Simulation and Safety, Tianjin University, Tianjin 300072, Chin
d Center of Excellence for Ocean Engineering, National Taiwan Ocean University, Keelung 202301, Taiwan

* Email address for correspondence: hkb.math@gmail.com (Harekrushna Behera)

https://doi.org/10.1063/5.0146004

Submitted: 09 February 2023 • Accepted: 25 March 2023 • Published Online: 12 April 2023

Role of dual breakwaters and trenches on efficiency of an oscillating water column

Nikita Naik[a], Siming Zheng (郑思明)[b,c], Harekrushna Behera[a,d,*]

[a]*Department of Mathematics, SRM Institute of Science and Technology, Kattankulathur, Tamil Nadu, India*
[b]*School of Engineering, Computing and Mathematics, University of Plymouth, Drake Circus, Plymouth, PL4 8AA, United Kingdom*
[c]*State Key Laboratory of Hydraulic Engineering Simulation and Safety, Tianjin University, Tianjin 300072, Chin*
[d]*Center of Excellence for Ocean Engineering, National Taiwan Ocean University, Keelung 202301, Taiwan*

Abstract

In this paper, the effects of double-submerged breakwaters and trenches on the hydrodynamic performance of an oscillating water column (OWC) are investigated. The multi-domain boundary element method is used to tackle the physical problem of wave scattering and radiation from the device. The role of the height of the breakwaters, depth of the trenches, width of the breakwaters and trenches, spacing between the structures, length of the OWC chamber, and other wave and structural parameters are investigated on the efficiency of OWC. The study reveals that there is an oscillating pattern of the efficiency curve in the presence of single or double breakwater/trenches; this pattern is absent when the bottom is flat. Moreover, compared to single or no breakwaters/trenches, the occurrence of full OWC efficiency is higher in the presence of double breakwaters/trenches. Furthermore, the amplitude of the oscillating pattern in the efficiency curve increases with an increase in the height and depth of the breakwaters and trenches, respectively. For some particular wave and structural parameters, zero OWC efficiency occurs nearly $k_0h = 3.4$ within $0 < k_0h < 5$ (k_0 wave number and h water depth). This zero efficiency moves towards small wave numbers as the spacing between OWC to rigid breakwater/trench increases. The radiation conductance of OWC decreases with increasing the barrier height. The findings outline the structural criteria that can be employed to build and deploy an effective OWC device.

Keywords: Oscillating water column; Submerged breakwaters; Trenches; Wave energy converter; Boundary element method.

1. Introduction

Renewable energy sources have gained interest as a possible sustainable energy alternative as a result of the depletion of resources like fossil fuels and its environmental collision with climate change and air pollution (Ozkop and Altas (2017) and Liu et al. (2019)). The World Energy Council estimates that the annual global wave energy is 17.5 PWh, which can be contrasted with the 16 PWh projected

*Corresponding Author
Email addresses: nikitanaikvssut@gmail.com (Nikita Naik), siming.zheng@plymouth.ac.uk (Siming Zheng (郑思明)), hkb.math@gmail.com (Harekrushna Behera)

annual global energy usage (Boyle (2004)). Many theoretical studies on wave energy have been conducted since the 1970s. Wave energy converters (WECs) have received a lot of attention, and many different designs are currently undergoing sea trials. Depending upon the working principle of WECs, they can be largely classified into oscillating water columns (OWCs) and oscillating bodies. OWC devices are among the fundamental ideas that initially appeared in the first decade of the nineteenth century, making them the first generation of devices (Rezanejad et al. (2013)). It contains an open-end box made up of concrete or steel, which is submerged partly in the water. Due to the incoming incident waves, the water column inside the chamber experiences alternate pressure variations. One of the key benefits of the OWC device is that by utilizing high-speed turbines, it is able to create electricity at a frequency that is significantly higher than the average wave frequency, which is in the order of 1-10 Hz. They can be considered as more privileged as compared to other existing devices (Rezanejad et al. (2013)). A review of the development of the coming age of OWC can be found in Heath (2012). Moreover, a complete review of the verified concepts, as well as designs of WECs, is delineated by Falnes (2007) and Antonio (2010).

To provide an overview, many researchers have focused on several analytical, numerical, and experimental investigations to understand the hydrodynamic performance of a single OWC device (Evans and Porter (1995), Şentürk and Özdamar (2011), Delmonte et al. (2014), Ning et al. (2015), Wang and Zhang (2021)). Evans and Porter (1995) looked at how OWC was able to extract power since the usual incident wave was pushing the fluid's free surface against the barrier and the wall. They observed that known reciprocal relations are satisfied identically, and the Galerkin approximation method can be used to obtain accurate values for all the frequencies, including the large values which are essential for time-domain modeling of non-linear power take-offs. In order to demonstrate the aerodynamic performance of a high-solidity Wells turbine for a wave power plant, Gato et al. (1996) conducted experimental research and presented the findings. By using a numerical simulation of the OWC performance, Brito-Melo et al. (2002) looked into the examination of the Wells turbine design parameters. The impact of the Wells turbine's aerodynamic design on the performance of the entire plant was also made clear by their study. A three-dimensional numerical model of a fixed OWC system by solving a steady-state potential flow boundary value problem was presented and validated by Delauré and Lewis (2003). Jalón and Brennan (2020) investigated the trade-off between structural durability and the device's energetic response in irregular waves by comparing the hydrodynamic efficiency of a stationary OWC device to its structural longevity. The hydrodynamic performance of an offshore OWC device mounted over an immersed horizontal plate was studied by Wang and Zhang (2021) with the employment of the open-source CFD toolbox OpenFOAM. It was reported that a smaller immersed depth of the plate was likely to provide more benefits for wave power extraction. Khan and Behera (2021) investigated the impact of sloping porous seabed on the efficiency of an OWC against oblique waves. They found that the OWC efficiency is highly sensitive to the slope of the porous seabed, and the seabed porosity stabilizes the resonant frequency against changes in water levels. Cui et al. (2021) investigated how much wave energy could be extracted from a hybrid oscillating water column oscillating buoy wave energy converter. As waves pass over the buoy, they notice that the water column within the OWC chamber travels up and down, creating airflow that

powers a turbine.

Apart from single OWC device consideration, there are many studies on the analysis of the hydrodynamic performance of dual-chamber OWC models (Wang et al. (2017), Ning et al. (2018), Ning et al. (2019) and Haghighi et al. (2021)). Non-linear 2D analysis of the efficiency of fixed OWC-WEC was studied by Luo et al. (2014). They observed that the thickness and seaward wall draft of the OWC device had a significant impact on the resonance frequency and the OWC's capture effectiveness. Ning et al. (2019) performed a study based on an experimental evaluation of a twin chamber land-based OWC wave energy converter; they found that the system's overall efficiency is insensitive and that a higher rate of wave energy absorption is caused by both the system's maximum efficiency and its range of wave frequencies. Wang et al. (2021) performed a number of theoretical investigations on the hydrodynamic performance of a dual-chamber OWC device with a pitching front lip wall using the matching eigenfunction approach. They found that when a device is designed with an asymmetry structure configuration, it is more desirable. Wang and Zhang (2022) investigated how a twin chamber OWC may perform better using side wall effects in small flumes. They came to the conclusion that the OWC system's performance in wave power extraction at various model-scale wave flume widths could vary. The analysis of OWC wave-power plants using a 3D boundary element code was investigated by Zhou et al. (2019). They discovered that the OWC's hydrodynamic performance could be enhanced in the high-frequency domain by using the suitable configuration of two sub-chambered drafts.

In addition to single and dual OWCs, numerous researchers have recently emphasized the hydrodynamic performance of multiple OWCs (Zheng et al. (2019), Howe et al. (2020), Kim and Nam (2022)). A multi-chamber OWC using cascaded savory turbines was studied by Dorrell et al. (2010). They came to the conclusion that the system is straightforward and reliable and would be appropriate for minor applications along shorelines where the waves are smaller and of lower amplitude. Shalby et al. (2016) investigated a multi-chamber OWC in a physical scale model. They observed the effects of the chamber on various OWC parameters along with the airflow rate in the duct. Furthermore, an analytical and numerical study of nearshore multiple OWCs was carried out by Rezanejad et al. (2016). Using linear potential theory and eigenfunction matching method Zheng et al. (2019) studied the wave power extraction from multiple OWCs along a straight coast. Zheng et al. (2020) studied the hydrodynamic efficiency of a multi-OWC platform. They noted that over the majority of the calculated range of wave circumstances, the multi-OWC platform with thinner walls performed better in terms of wave power extraction.

On the other hand, for the purpose of identifying natural occurrences like seiches or free surface oscillations, the study of Bragg resonance is essential. The sea surface rises and falls as a result of this process, which frequently causes an increase in wave amplitude over time. Due to the effects of shoaling, refraction, diffraction, and reflection, the wave patterns that develop on the water's surface go through many transformations. Since last few decades, there are many studies available in the literature on Bragg scattering by double or multiple breakwaters/trenches in the absence of OWC (Ting and Raichlen (1986), Kar et al. (2019), Gao et al. (2021)). Ting and Raichlen (1986)) looked at how typically occurring water waves propagated via a rectangular sectioned submarine trench. A

study concerning the scattering of surface gravity waves over a pair of trenches was investigated by Kar et al. (2018). They discovered that as trench width increases, wave reflection falls off oscillatory. Recently, a study regarding Bragg scattering of long waves by an array of trenches was perceived by Kar et al. (2020). Their investigation shows that, as opposed to trenches with uniform or sloping seabeds, those with a shift in seabed slope result in a bigger Bragg's reflection.

Over the past few decades, apart from different mathematical techniques, the boundary element method (BEM) has been developed and extensively used by many researchers for various physical models (Wang and Meylan (2002), Payne et al. (2008), Yueh and Chuang (2012), Meylan and Fitzgerald (2014), Meylan et al. (2017), Khan and Behera (2020), Vijay et al. (2022)). Mackerle and Andersson (1984) reviewed the applications of the boundary element method to the solution of a wide variety of problems in engineering. A comprehensive review of boundary element methods for hydrodynamic modeling of wave energy systems was suggested by Papillon et al. (2020). They presented some background to each aspect of the boundary methods reviewed, building up a relatively complete theoretical framework. Wang and Meylan (2002) studied the linear wave responses of a floating thin plate on the water of variable depth using the boundary element method. Yueh and Chuang (2012) analyzed the effectiveness of a partially piston-type porous wave energy converter using the multi-domain BEM. They developed a single-degree-of-freedom system to describe the response of the WEC. Liu et al. (2016) used an extremely efficient boundary element method for wave interaction with long cylindrical structures based on free-surface Green's function. They used a higher-order scheme to discretize the geometry of the structure as well as the physical wave potentials. Kar et al. (2019) suggested a numerical model using the boundary element method to analyze gravity wave transformation by a finite floating dock in the presence of bottom undulation such as trenches, breakwaters, and a combination of both in two dimensions. Khan et al. (2021) used the boundary element method for wave trapping by a multi-layered trapezoidal breakwater near a sloping rigid wall. Mathematical modeling of breakwater-integrated oscillating water column wave energy converter devices under irregular incident waves was studied by Trivedi and Koley (2021) using the boundary element method. In most of these studies, the potential flow is considered to tackle the physical problem. It is worth to be mentioned that the potential-flow formulation is quite reasonable, prudence is always necessary because the effects that are ignored are most significant near the body surface. It is often an excellent approximation to real flow (Hess and Smith (1967), Hess (1973)).

Although there are some studies on the effects of breakwaters on the performance of OWC (Park et al. (2018), Deng et al. (2014), Park et al. (2019), Deng et al. (2020, 2021)), to the authors' knowledge, no research has been done on coupled breakwaters/trenches and OWC. Breakwaters and trenches can be employed as protective structures to lessen the wave force on the wave chamber barrier and the end wall as well as to achieve full OWC efficiency through the oscillation between the structures. Thus, the present study aims to analyze the effects of breakwaters and trenches on the efficiency of OWC by using the multi-domain boundary element method. The present manuscript is arranged as follows: The detailed mathematical formulation is described in Section 2. Section 3 discusses the parameters related to the OWC device's performance. In Section 4, the solution of the mathematical model using the dual boundary element method is presented. The validation of

the present solution and the role of all wave structural parameters on the efficiency of the OWC are analyzed in Section 5. Finally, the conclusions of the present investigation are described in Section 8.

2. Mathematical formulation

In the present section, mathematical formulation for the hydrodynamic performance of an OWC device in the presence of a pair of rigid breakwaters and trenches is discussed in finite water depth under small amplitude water wave theory. A three-dimensional Cartesian coordinate system (x, y, z) is used to construct the associated physical model, with the $x - y$ plane parallel to the free surface and the z axis being in the vertical upward negative direction. The OWC device is modeled as a thin surface-piercing vertical plate of immersion depth L_8, placed at $x = 0$, near a rigid wall (as shown in Fig. 1). Further, a_1 and a_2 are heights, and b_1 and b_2 are the widths of the first and second breakwater respectively. The same parameters are also considered for the first and second trenches' depth and width as well as shown in Fig. 2. The spacing between two breakwaters, second structure to OWC, and OWC to the rigid wall are denoted as L_4, L_6 and L_{10} respectively. The fluid is considered inviscid and incompressible, and the motion is irrotational. Moreover, the time-harmonic motion of waves with angular velocity ω is employed. The fluid domain is restricted by an auxiliary boundary $x = -r_0$ to simplify the domain construction. The resulting flow domain is predominantly divided into two regions, namely R_1 and R_2, consisting of virtual boundaries: $R_1 = \{(x, y) \in L_1 \cup L_2 \cup L_3 \cup L_4 \cup L_5 \cup L_6 \cup L_7 \cup L_8 \cup L_9\}$ and $R_2 = \{(x, y) \in L_8 \cup L_7 \cup L_{10} \cup L_{11} \cup L_{12}\}$, respectively. The fluid properties are characterized by scalar velocity potential $\Phi(x, y, z, t)$, which satisfies $\nabla^2\Phi = 0$. Thus, the existing a velocity potential $\Phi(x, z, t)$, that takes the following form $\Re\{\phi_j(x, z)e^{-\mathrm{i}(k_y y-\omega t)}\}$, where $\phi_j(x, z)$ is the complex-valued spatial potentials, $\Re$ denotes the real part, $j = 1, 2$ and $k_y = k_0 \sin\theta$, where k_0 is the progressive wave number, θ is the incident wave angle. The spatial component of velocity potential satisfies the Helmholtz equation,

$$(\partial_{xx} + \partial_{zz} - k_y^2)\phi_j = 0, \quad \forall j. \tag{1}$$

As the present physical model is based on the boundary element method, the corresponding boundary conditions can be described as follows. The boundary conditions at the mean free surface $(L_9 \cup L_{12})$ is defined as

$$\frac{\partial\phi_1}{\partial z} - K\phi_1 = 0, \quad \text{at } L_9, \tag{2}$$

$$\frac{\partial\phi_2}{\partial z} - K\phi_2 = \frac{\mathrm{i}\omega p}{\rho g}, \quad \text{at } L_{12}, \tag{3}$$

where $K = \dfrac{\omega^2}{g}$ with g be the acceleration due to gravity. The pressure distributed over the internal free surfaces is given as

$$\mathcal{P}(t) = \Re\{pe^{-\mathrm{i}\omega t}\}, \tag{4}$$

where p is the complex amplitude of the pressure inside the OWC chamber. The zero flux through the impermeable sea bed, OWC, and the wall can be written as

$$\frac{\partial\phi_j}{\partial \boldsymbol{n}} = 0, \quad \text{at} \quad L_2,\ L_3,\ L_4,\ L_5,\ L_6,\ L_8\ L_{10},\ L_{11}, \quad \text{for} \quad j = 1, 2. \tag{5}$$

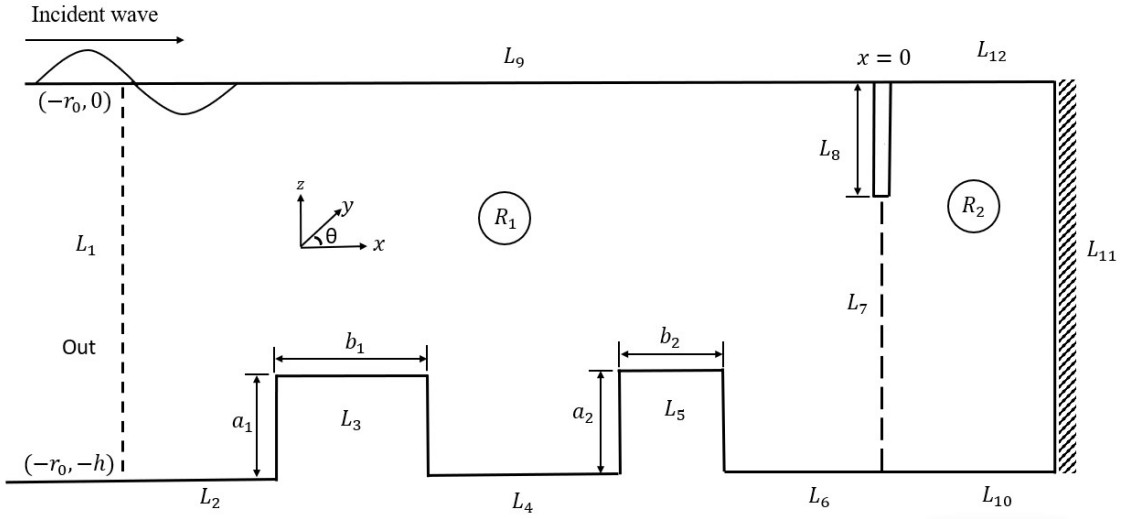

Figure 1: Schematic representation of single chambered OWC-WEC in the presence of double breakwaters

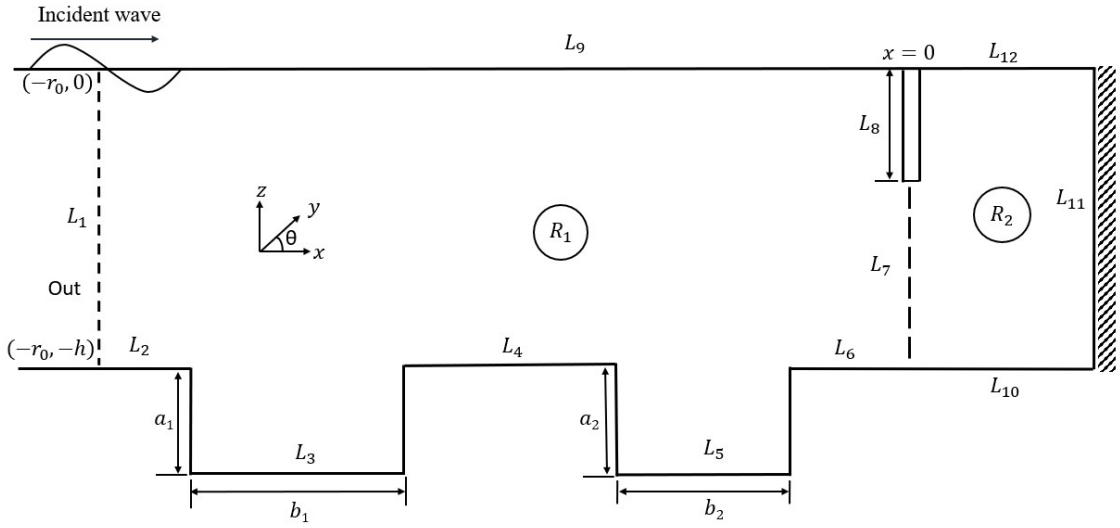

Figure 2: Schematic representation of single chambered OWC-WEC in the presence of double trenches

The continuity of velocity and pressure at the virtual boundary L_7 can be written as

$$\frac{\partial \phi_1}{\partial x} = \frac{\partial \phi_2}{\partial x}, \quad \phi_1 = \phi_2. \tag{6}$$

It is to be eminent that the velocity potential includes scattered and radiated velocity potential. As a result, the total velocity potential can be defined as

$$\phi_j = \phi_j^S + \phi_j^R, \quad \forall j, \tag{7}$$

where the scattered potential is denoted by ϕ_j^S and the radiated potential by ϕ_j^R. The far-field conditions are governed by

$$\phi_1^R(x,z) = \mathcal{A}_0^R e^{-\mathrm{i}\mu_0(x+r_0)} f_0(k_0,z), \quad x \to -\infty, \tag{8}$$

$$\phi_1^S(x,z) = (e^{\mathrm{i}\mu_0(x-b)} + \mathcal{A}_0^S e^{-\mathrm{i}\mu_0(x+r_0)}) f_0(k_0,z), \quad x \to -\infty, \tag{9}$$

where $\mathcal{A}_0^S$ and $\mathcal{A}_0^R$ are the reflected and radiated wave amplitudes. Moreover, $f_0(k_0, z) = \left(\frac{\mathrm{i}g}{\omega}\right)\frac{\cosh k_0(z+h)}{\cosh k_0 h}$ is the eigenfunction in the open water region with $\mu_0 = \sqrt{{k_0}^2 - {k_y}^2}$.

3. OWC governing parameters

This section contains the expressions for several physical parameters related to the functionality of the OWC device. The internal free surface time-harmonic induced volume flux is given as

$$q = \int_{L_{12}} \frac{\partial \phi}{\partial z} dx = q^S - \frac{\mathrm{i}\omega p}{\rho g} q^R, \tag{10}$$

where q^S and q^R being the volume flux across the internal free surface L_{12} in the scattering and radiation problems, respectively. The volume flux required for the radiation potential is given as

$$\frac{\mathrm{i}\omega p}{\rho g} q^R = -(\tilde{\beta} - \mathrm{i}\tilde{\gamma})p, \tag{11}$$

where $\tilde{\beta}$ and $\tilde{\gamma}$ are analogous to added mass and damping coefficient called radiation susceptance and conductance parameters

$$\tilde{\gamma} = \frac{\omega}{\rho g}\Re\{q^R\}, \quad \tilde{\beta} = \frac{\omega}{\rho g}\Im\{q^R\}, \tag{12}$$

where $\Im$ is the imaginary part. The volume flux through the turbine is linearly proportional to the pressure drop across the internal free surface and hence

$$q = \Lambda p, \tag{13}$$

where Λ is the real positive constant and is termed as the control parameter. Along with volume flux, the mean rate of work done by the pressure for one wave period is defined as (Khan and Behera (2021))

$$W = \frac{|q_s|^2}{2}\frac{\Lambda}{(\Lambda + \tilde{\beta})^2 + \tilde{\gamma}^2}. \tag{14}$$

For some known values $\tilde{\gamma}$ and $\tilde{\beta}$ the observed optimum values can be described as follows

$$\Lambda_{opt} = \sqrt{\tilde{\gamma}^2 + \tilde{\beta}^2}. \tag{15}$$

Therefore, the pressure force results in the maximum work done narrate the below equation

$$W_{max} = \frac{|q_s|^2}{4}\frac{1}{\Lambda_{opt} + \tilde{\beta}}. \tag{16}$$

The transported wave power per unit width of the wavefront of the undisturbed incident waves, which is represented as (Dean and Dalrymple (1991))

$$\mathcal{P}_W = \mathscr{E}_W c_g, \quad \mathscr{E}_W = \frac{\rho g}{2}, \quad c_g = \frac{\omega}{2k_0}\left(1 + \frac{2k_0 h}{\sinh 2k_0 h}\right), \tag{17}$$

where $\mathscr{E}_W$ denotes the total energy per wave period along with this c_g represents the group velocity. Similarly, the efficiency of the OWC-WEC system is defined by

$$\eta_{max} = \frac{W_{max}}{\mathcal{P}_W}. \tag{18}$$

The non-dimensional parameters ν and μ are used to represent the radiation conductance and susceptibility as

$$\nu = \frac{\rho g}{\omega b}\tilde{\beta}, \quad \mu = \frac{\rho g}{\omega b}\tilde{\gamma}. \tag{19}$$

The following formula provides the OWC device's maximum power absorption efficiency:

$$\eta = \frac{2}{\left(1 + \left(\frac{\mu}{\nu}\right)^2\right)^{\frac{1}{2}} + 1}. \tag{20}$$

4. Method of solution

For the domains R_1 and R_2, the aforementioned boundary value problem is addressed using the linked eigenfunction expansion technique and multi-domain boundary element method. Instead of using BEM alone, the boundary element formulation is used for a comparatively smaller region, and the semi-analytic eigenfunction expansion technique is employed for the semi-infinite outer region. As a consequence, the methodology for getting the solution is computationally more efficient.

4.1. Eigenfunction expansion method

The velocity potential in the outer region can be expressed as

$$\phi^R_{\text{out}}(x,z) = \sum_{n=0}^{\infty} \mathcal{A}^R_n e^{-\mathrm{i}\mu_n(x+r_0)} f_n(k_n,z), \quad x \to -\infty, \tag{21}$$

$$\phi^S_{\text{out}}(x,z) = e^{\mathrm{i}\mu_n(x+r_0)} f_0(z) + \sum_{n=1}^{\infty} \mathcal{A}^S_n e^{-\mathrm{i}\mu_n(x+r_0)} f_n(z), \quad x \to -\infty. \tag{22}$$

In the above equations, $\mu_n = \sqrt{{k_n}^2 - {k_y}^2}$ where k_n satisfy the dispersion equation

$$K = k_n \tanh(k_n h). \tag{23}$$

Furthermore, eigenfunction $f_n(k_n, z)$ is given by

$$f_n(k_n,z) = \left(\frac{\mathrm{i}g}{\omega}\right)\frac{\cosh k_n(z+h)}{\cosh k_n h}. \tag{24}$$

The properties of the orthogonality in eigenfunctions are written as

$$\int_0^h f_n(k_n,z) f_m(k_n,z) dz = \mathscr{I}_n \delta_{mn}, \tag{25}$$

where $\mathscr{I}_n = \int_{-h}^{0} f_n^2(k_n, z)dz = -\left(\frac{g^2}{\omega^2}\right)\frac{k_n h + \sin(k_n h)\cos(k_n h)}{2k_n \cos(k_n h)}$ and δ_{mn} is the Kronecker delta. Furthermore, $\mathcal{A}_n^S$ and $\mathcal{A}_n^R$ are defined as

$$\mathcal{A}_n^R = \frac{1}{\mathscr{I}_n}\int_{-h}^{0} \phi_{\text{out}}^R(z)|_{x=-r_0} f_n(k_n, z)dz, \tag{26}$$

$$\mathcal{A}_n^S = -\delta_{n0} + \frac{1}{\mathscr{I}_n}\int_{-h}^{0} \phi_{\text{out}}^S(z)|_{x=-r_0} f_n(k_n, z)dz. \tag{27}$$

After truncating the infinite series after the $\mathscr{N}$ terms and applying $\mathcal{A}_n^R$ and $\mathcal{A}_n^S$, the normal derivative of the potentials in Eqs. (23) and (24) is given as

$$\left.\frac{\phi_{\text{out}}^R}{\partial \mathbf{n}}\right|_{x=-r_0} = -\sum_{n=0}^{\mathscr{N}} \frac{\mathrm{i}\mu_n}{\mathscr{I}_n}\left\{\int_{-h}^{0} \phi_{\text{out}}^R(s)\,\psi_n(k_n,\ s)\,ds\right\} f_n(k_n, z), \tag{28}$$

$$\left.\frac{\phi_{\text{out}}^S}{\partial \mathbf{n}}\right|_{x=-r_0} = -2\mathrm{i}\mu_0 f_0(k_0,\ z) + \sum_{n=0}^{\mathscr{N}} \frac{\mathrm{i}\mu_n}{\mathscr{I}_n}\left\{\int_{-h}^{0} \phi_{\text{out}}^S(s)\, f_n(k_n,\ s)\,ds\right\} f_n(k_n,\ z). \tag{29}$$

4.2. Boundary element method

Upon applying Green's integral theorem to Eq. (1) and by exploiting Green's function G, the corresponding integral equation can be denoted as,

$$-\begin{pmatrix} \phi(\xi,\eta) \\ \frac{1}{2}\phi(\xi,\eta) \end{pmatrix} = \int_\Gamma \left(\phi\frac{\partial \mathcal{G}}{\partial \mathbf{n}}(x,z;\xi,\eta) - \mathcal{G}(x,z;\xi,\eta)\frac{\partial \phi}{\partial \mathbf{n}}\right)d\Gamma, \begin{pmatrix} \text{if } (x,z) \in \text{int}(\Gamma) \\ \text{if } (x,z) \in \Gamma \end{pmatrix}, \tag{30}$$

On the boundary, Γ, the aforementioned (ξ, η) is the source point, (x, z) is the field point, and $\mathbf{n}$ is the outward normal. Moreover, Green's function is estimated from the fundamental solution of the equation (Gayathri et al. (2022))

$$(\nabla^2 - k_y)\mathcal{G} = \delta(\xi - x)\delta(\eta - z); \quad \mathcal{G}(x,z;\xi,\eta) = \frac{\xi_0\left(k_y r\right)}{2\pi} \quad \text{where} \quad r = \sqrt{(\xi - x)^2 + (\eta - z)^2} \tag{31}$$

The above symbolized ξ is the modified zeroth-order Bessel function of the second kind. $r \to 0$, one obtains the asymptotic behavior,

$$\chi_0(k_y r) = -\gamma - \ln\left(\frac{k_y r}{2}\right), \tag{32}$$

where $\gamma = 0.5772$ is the preferable Euler's constant. After implementing the boundary conditions in the defined region R_1 and R_2 and presuming constant velocity potential on each of the boundary

elements, the following system of integral equations can be obtained.

$$c\phi_1 + \int_{L_1}\Big(\phi_1\partial_n\mathcal{G} - \mathcal{G}\partial_n\varphi_1\Big)dL + \int_{L_2}\phi_1\partial_n\mathcal{G}dL + \int_{L_3}\phi_1\partial_n\mathcal{G}dL + \int_{L_4}\phi_1\partial_n\mathcal{G}dL + \int_{L_5}\phi_1\partial_n\mathcal{G}dL + \int_{L_6}\phi_1\partial_n\mathcal{G}dL + \int_{L_7}\Big(\phi_1\partial_n\mathcal{G} - \mathcal{G}\partial_n\phi_1\Big)dL + \int_{L_8}\phi_1\partial_n\mathcal{G}dL + \int_{L_9}\phi_1\Big(\partial_n\mathcal{G} - K\mathcal{G}\Big)dL = 0 \tag{33}$$

$$c\phi_2 + \int_{L_8}\phi_2\partial_n\mathcal{G}dL + \int_{L_7}\Big(\phi_2\partial_n\mathcal{G} - \mathcal{G}\partial_n\phi_2\Big)dL + \int_{L_{10}}\phi_2\partial_n\mathcal{G}dL + + \int_{L_{11}}\phi_2\partial_n\mathcal{G}dL + \int_{L_{12}}\phi_2\Big(\partial_n\mathcal{G} - K\mathcal{G}\Big)dL = 0 \tag{34}$$

For each region, a system of equations can be achieved for the elements on discretized boundaries, integrated with the postulation of constant potential across each boundary element which consequences the matrix equation like $\boldsymbol{H}\mathcal{U} = \boldsymbol{G}\boldsymbol{Q} + \boldsymbol{B}$, where

$$\boldsymbol{H} = \begin{bmatrix} \Omega & H^1_{L_2} & H^1_{L_3} & H^1_{L_4} & H^1_{L_5} & H^1_{L_6} & H^1_{L_7} & H^1_{L_8} & \mathscr{B}_{L_9} & 0 & 0 & 0 \\ 0 & 0 & 0 & 0 & 0 & 0 & H^2_{L_7} & H^2_{L_8} & 0 & H^2_{L_{10}} & H^2_{L_{11}} & \mathscr{B}^2_{L_{12}} \end{bmatrix}, \tag{35}$$

$$\mathcal{U} = \begin{bmatrix} U^1_{L_1} & U^1_{L_2} & U^1_{L_3} & U^1_{L_4} & U^1_{L_5} & U^1_{L_6} & U^1_{L_7} & U^1_{L_8} & U^1_{L_9} & U^2_{L_{10}} & U^2_{L_{11}} & U^2_{L_{12}} \end{bmatrix}^T, \tag{36}$$

$$\boldsymbol{B} = \begin{cases} \begin{bmatrix} -2\mathrm{i}\mu\mathscr{A}^S & 0 & 0 & 0 & 0 & 0 & 0 & 0 & 0 & 0 & 0 & 0 \end{bmatrix}^T & \text{for scattered potential,} \\ \begin{bmatrix} 0 & 0 & 0 & 0 & 0 & 0 & 0 & 0 & 0 & 0 & 0 & -\dfrac{\mathrm{i}\omega p}{\rho g} \end{bmatrix}^T & \text{for radiated potential.} \end{cases} \tag{37}$$

where $\mathscr{B}^1_{L_9} = (H^1 - K\mathcal{G}^1)_{L_9}$, $\mathscr{B}^2_{L_{12}} = (H^2 - K\mathcal{G}^2)_{L_{12}}$, $H^i_j = C\delta_{ij} + \int_{L_j}\partial_{\mathbf{n}}\mathcal{G}\,dL$, $\mathcal{G}^i_j = \int_{L_j}\mathcal{G}\,dL$, $\mathcal{U}^i_j = \phi^i_j$

$$\Omega = \begin{cases} \displaystyle\sum_{n=0}^{\mathcal{N}}\frac{\mathrm{i}\mu_n}{\mathcal{T}_n}\left\{\int_{-h}^{0}\phi^S_{\text{out}}(s)\,f_n(k_n,\,s)\,ds\right\}f_n(k_n,\,z), & \text{for scattered potential,} \\ \displaystyle-\sum_{n=0}^{\mathcal{N}}\frac{\mathrm{i}\mu_n}{\mathcal{T}_n}\left\{\int_{-h}^{0}\phi^R_{\text{out}}(s)\,f_n(k_n,\,s)\,ds\right\}f_n(k_n,\,z), & \text{for radiated potential.} \end{cases} \tag{38}$$

The two coefficients H^i_j and G^i_j are evaluated using numerical integration. Therefore, by solving the aforementioned set of equations, the potential and flux values in the respective boundaries are obtained.

5. Results and discussions

In this section, by using MATLAB 2021a, several results associated with the performances of an OWC device are plotted and discussed in a detailed manner. Unless otherwise specified, the following

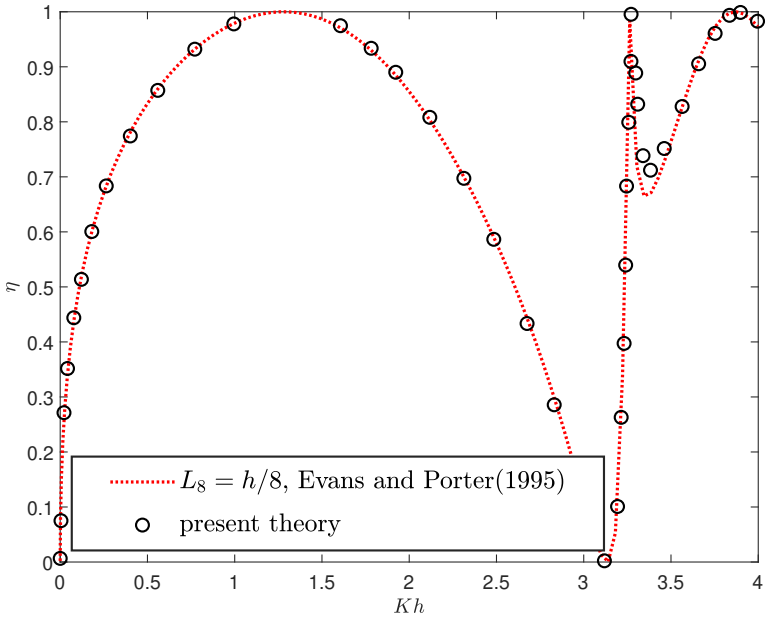

Figure 3: Comparison of present study with Evans and Porter (1995) for $L_8/h = 1/8$ with $\theta = 0°$, $h = 4$, $L_{10}/h = 1$ and $a_1/h = a_2/h = 0$.

physical parameters are fixed in the computation: water depth $h = 4$ m, height/depth of the breakwater $a_1/h = a_2/h = 0.2$, trench $a_1/h = a_2/h = 0.6$, incident angle $\theta = 20°$, $L_8/h = 0.2$, and $L_{10}/h = 1$. Moreover, it should be mentioned that various resonance mechanisms that take place inside the OWC have a significant impact on the efficiency of the device. The details of the mechanics can be found in Rezanejad et al. (2013) and Rezanejad et al. (2015).

5.1. Validation

It is worth noting that for $a_1/h = a_2/h = 0$ (absence of breakwaters and trenches), the present physical model becomes the model of Evans and Porter (1995). To check the perfection of the results of present numerical computations, in Fig. 3, the maximum efficiency η against Kh is plotted in the absence of breakwaters/trenches with the same wave and structural parameters considered by Evans and Porter (1995) for a single chambered OWC in a flat bottom. It can be seen that the present result is well matched with the result of Evans and Porter (1995). The impacts of different wave and structural characteristics on the effectiveness of OWC are investigated individually in the sections that follow when double breakwaters and trenches are present.

5.2. Effects of double bottom-standing rigid breakwaters

The maximum OWC efficiency against non-dimensional wave number (k_0h) is shown in Fig. 4(a) for three different scenarios: without a breakwater, with a single breakwater, and with double breakwaters. It is observed that in the case of the flat bottom (absence of breakwaters), there is no oscillating pattern of efficiency, whereas, in the presence of a single breakwater, there is a small oscillating pattern. Further, in the case of double breakwaters, the oscillating pattern seems more as compared to

that for the single breakwater. The occurrence of full OWC efficiency is more in the presence of double breakwaters as compared to that for single or absence of breakwaters. Moreover, for all these three cases, full efficiency occurs at $k_0h \approx 1.5$; however, at $k_0h \approx 3.4$, zero efficiencies occur. It may be concluded that the presence of double breakwaters can considerably affect the efficiency of OWC. The maximum OWC efficiency against non-dimensional wave number (k_0h) is shown in Fig. 4(a) for three different scenarios: without a breakwater, with a single breakwater, and with double breakwaters. It is observed that in the case of the flat bottom (absence of breakwaters), there is no oscillating pattern of efficiency, whereas, in the presence of a single breakwater, there is a small oscillating pattern. Further, in the case of double breakwaters, the oscillating pattern seems more as compared to that for the single breakwater. The presence of double breakwaters can considerably affect the efficiency of OWC. Similarly, panel 4(b) depicts the results for efficiency (η) against non-dimensional wave number (k_0h) for different values of height of two bottom-standing breakwaters ($a_1/h = a_2/h$). It is noticed that when the height of the structures increases, the amplitude of the efficiency curve increases gradually. As described in Fig. 4(a), the drop in efficiency occurs when $k_0h \approx 3.4$. After that, again, the efficiency increases and attains the maximum peaks. Therefore, the height of the breakwaters plays a major role in the hydrodynamic performance of the OWC device.

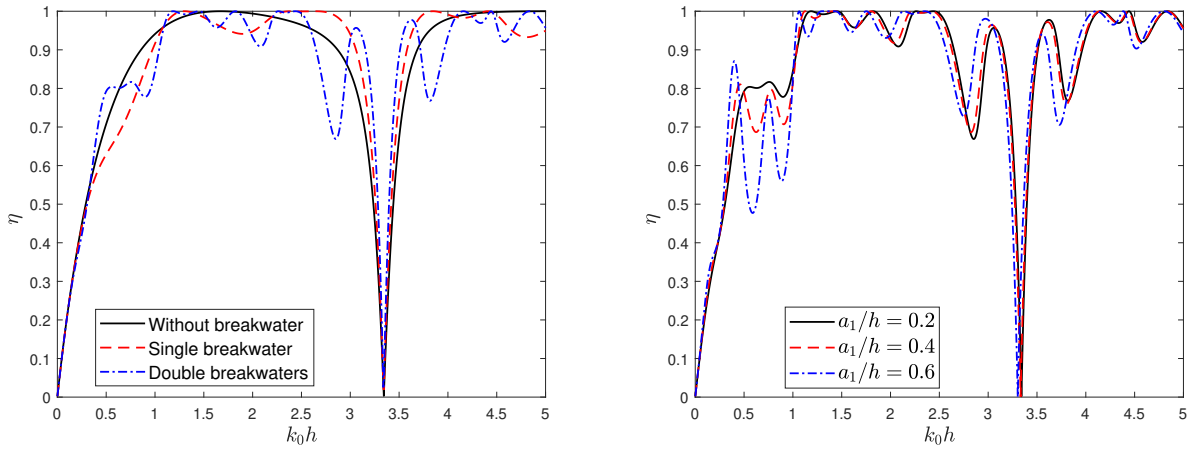

(a) (b)

Figure 4: (a) Maximum efficiency of OWC (η) versus non-dimensional wavenumbers (k_0h): (a) in the absence of breakwaters ($a_1/h = a_2/h \to 0$), presence of single ($a_1/h = 0.2$, $a_2/h \to 0$) and double breakwaters ($a_1/h = a_2/h = 0.2$) and (b) for different values of $a_1/h = a_2/h$. The other fixed parameters are $L_8/h = 0.2$, $b_1/h = b_2/h = 1$, $L_{10}/h = 1$, $L_4/h = 5$, $L_6/h = 2$, $L_2/h = 2$ and $\theta = 20°$.

Fig. 5(a) depicts the result for maximum efficiency (η) against non-dimensional wave number (k_0h) for various lengths of the barrier (L_8/h). It is observed that the efficiency of OWC increases with an increase in the length of the barrier. The cause of this phenomenon is that when the resonance frequency of the water column inside the OWC system is identical to the frequency of the incoming waves, the maximum amount of power absorption can be achieved in the chamber. Additionally, it is predicted that more water particles would traverse a greater distance within the OWC chamber during one oscillation cycle as the barrier's length increases. Moreover, the motion of the water column in

the OWC device is considered to be a resonant piston-like motion (Rezanejad et al. (2013)). However, there is no effect of other resonance mechanisms on efficiency. The increased length of the barrier begins to be prominent; consequently, the occurrence of other resonance close to the first one leads to an almost uniform high-efficiency range for OWC close to 1. The amplitude of the oscillatory efficiency curve is more for a smaller barrier height. The effect of spacing between the barrier to the rigid wall on the efficiency of OWC is presented in Fig. 5(b). It is seen that zero efficiencies occur multiple times for larger OWC width L_{10}/h. Moreover, owing to the presence of the vertical wall, the motion and pressure-dependent hydrodynamic coefficients of the OWCs are enhanced for some wave frequencies and moderated at the different ranges of frequencies. Consequently, it can be contemplated that the existence of a wall will influence the device's motions and efficiency in wave energy absorption. For a smaller OWC width (L_{10}/h), the efficiency grows exponentially with an increase in k_0h and results multiple times full efficiency.

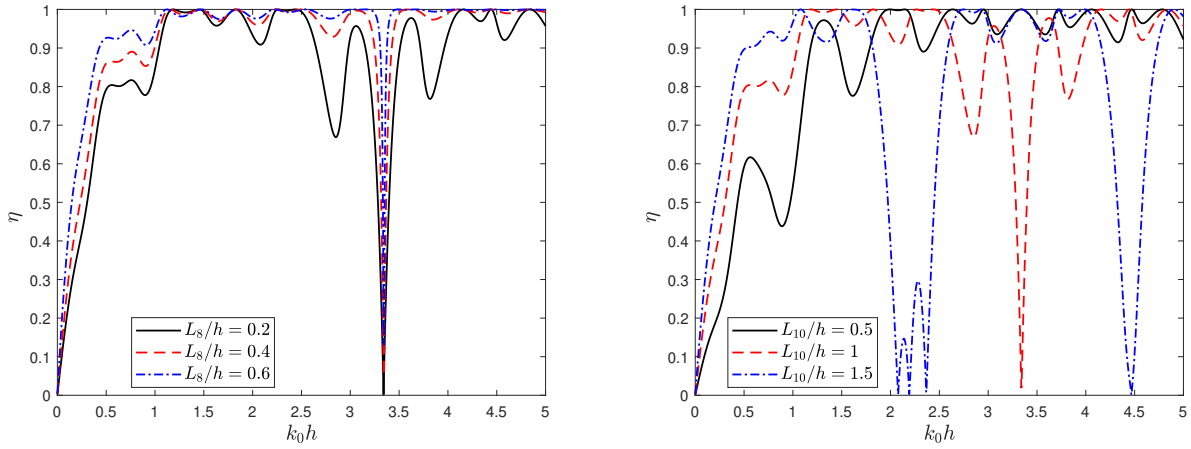

(a) (b)

Figure 5: Maximum efficiency of OWC (η) versus non-dimensional wavenumber (k_0h) for various (a) lengths of the barrier (L_8/h) with $L_{10}/h = 1$, and (b) spacing between OWC to rigid wall L_{10}/h with $L_8/h = 0.2$. The other fixed parameters are $a_1/h = a_2/h = 0.2$, $b_1/h = b_2/h = 1$, $L_4/h = 5$, $L_6/h = 2$, $L_2/h = 2$ and $\theta = 20°$.

Fig. 6(a) illustrates the result for maximum efficiency (η) against non-dimensional wavenumber (k_0h) for different values of width of the breakwaters ($b_1/h = b_2/h$). The figure reveals that the amplitude of the oscillatory pattern decreases with an increase in the values of the breakwaters' width. This may happen due to piston-like motion. Moreover, there is a left shifting of the optima of efficiency for increasing the width of the breakwaters due to phase shifting between the incident and reflected waves. As observed in Fig. 5(a), in this case also zero efficiencies occur for $k_0h \approx 3.4$. On the other hand, the role of spacing between the second breakwater and OWC (L_6/h) is analyzed in Fig. 6(b). It can be noted that there is a left shifting of optima of the efficiency curve with an increase in spacing between breakwater and OWC. For $k_0h < 0.5$, there are no changes found in the efficiency curve. Furthermore, nearly zero efficiencies occur and show a left shifting with increases in L_6/h.

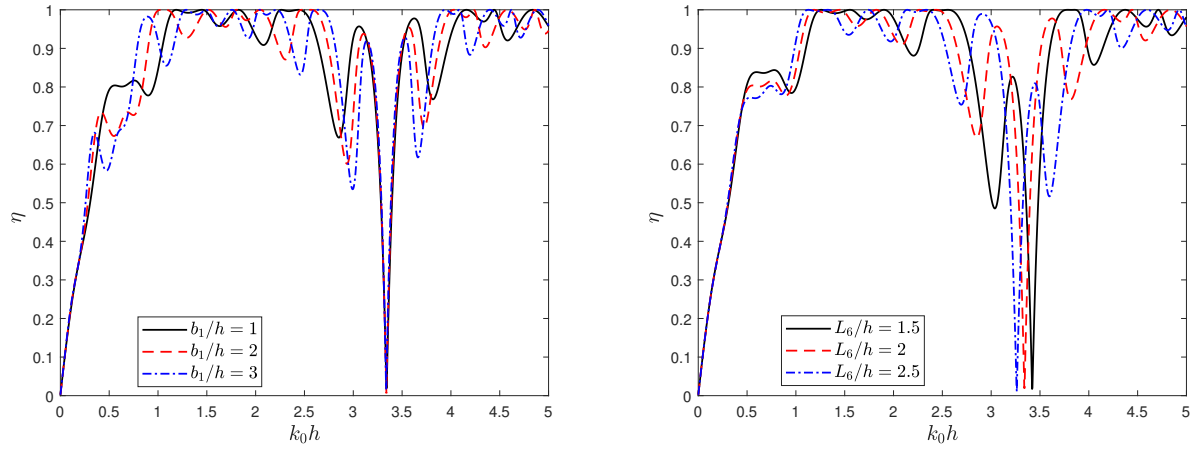

(a) (b)

Figure 6: Maximum efficiency of OWC (η) against non-dimensional wavenumber (k_0h) for various (a) widths of the breakwater ($b_1/h = b_2/h$) with $L_6/h = 2$, and (b) spacing between OWC to rigid breakwater (L_6/h) with $b_1/h = b_2/h = 1$. The other fixed parameters are $L_8/h = 0.2$, $a_1/h = a_2/h = 0.2$, $L_{10}/h = 1$, $L_4/h = 5$, $L_2/h = 2$ and $\theta = 20°$.

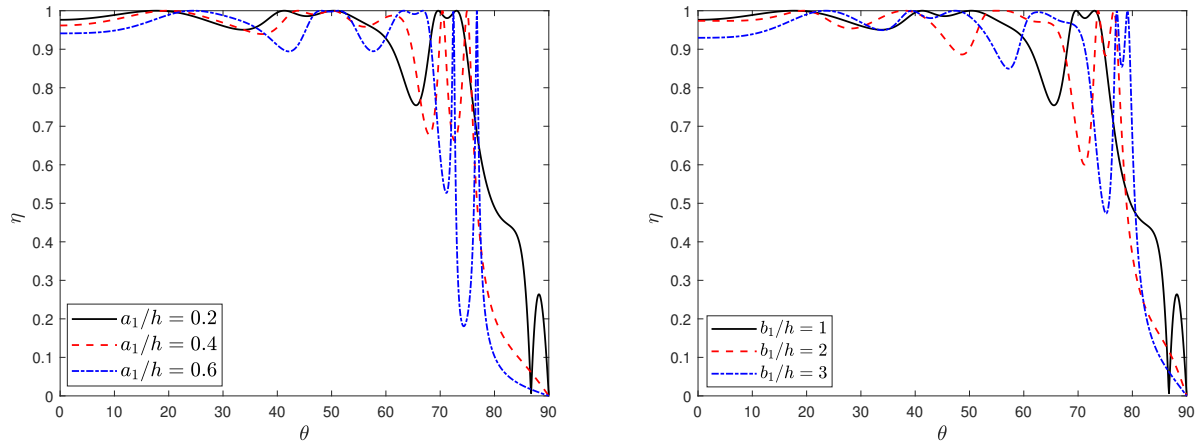

(a) (b)

Figure 7: Maximum efficiency of OWC (η) versus incident wave angle (θ) for various (a) heights of the breakwaters ($a_1/h = a_2/h$) with $b_1/h = b_2/h = 1$, and (b) widths of the breakwater ($b_1/h = b_2/h$) with $a_1/h = a_2/h = 0.2$. The other fixed parameters are $L_8/h = 0.2$, $L_{10}/h = 1$, $L_6/h = 2$, $L_4/h = 5$, $L_2/h = 2$ and k_0h=1.8.

The impact of the different heights of the breakwaters on the efficiency of the OWC device over the range of angle of incidence is plotted in Fig. 7(a). Careful observation demonstrates that as the height of the breakwaters increases, the efficiency of OWC (η) decreases for $\theta < 30°$. Moreover, zero efficiencies occur at $\theta = 90°$ irrespective of all other wave and structural parameters. At first full efficiency occurs for the smaller values of θ and height of the breakwater, which is due to the sloshing resonance mechanism with sloshing mode number $n = 1$. More oscillation in the efficiency curve was found for a larger value of $a_1/h = a_2/h$. The amplitude of the oscillatory curves rises for increasing

the height of the breakwaters. Similarly, Fig. 7(b) shows the relationship for maximum efficiency (η) against different incident wave angles (θ) for various widths of the breakwaters. As explained in Fig. 7(a), in this case, multiple times full efficiencies occur for the larger width of the breakwaters. The amplitude of the oscillatory pattern decreases and attains a right shifting for $\theta > 60^\circ$ with an increase in the width of the breakwaters.

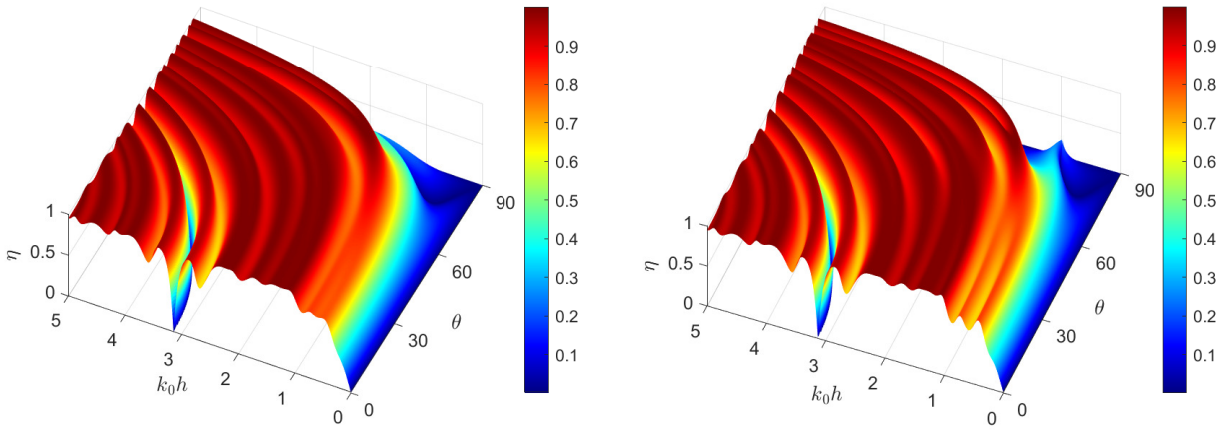

(a) $a_1/h = a_2/h = 0.2$ (b) $a_1/h = a_2/h = 0.4$

Figure 8: Surface plot of efficiency (η) against non-dimensional wavenumber (k_0h) and incident wave angle (θ) for various height of the breakwaters. The other fixed parameters are $L_8/h = 0.2$, $b_1/h = b_2/h = 1$, $L_6/h = 2$, $L_{10}/h = 1$, $L_4/h = 5$ and $L_2/h = 2$.

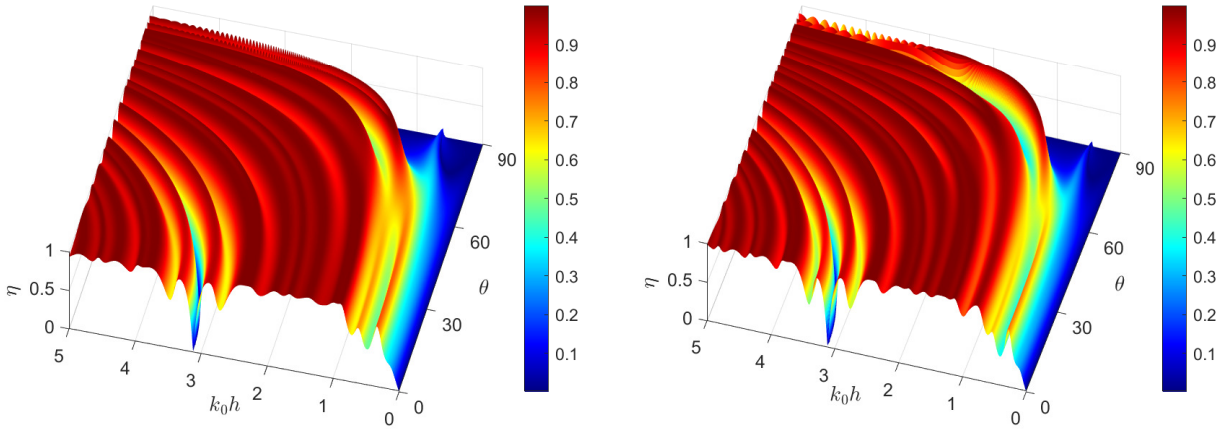

(a) $b_1/h = b_2/h = 2$ (b) $b_1/h = b_2/h = 3$

Figure 9: Surface plot of efficiency (η) against non-dimensional wavenumber (k_0h) and incident wave angle (θ) for various width of the breakwater. The other fixed parameters are $L_8/h = 0.2$, $a_1/h = a_2/h = 0.2$, $L_6/h = 2$, $L_{10}/h = 1$, $L_4/h = 5$ and $L_2/h = 2$.

In Fig. 8, the surface plot illustrates the efficiency coefficient (η) for varying values of (k_0h, θ). For larger heights of the breakwaters (Fig. 8(b)), it can be noticed that there is more oscillating pattern

in the efficiency curve as compared to the smaller height of the breakwater (Fig. 8(a)). Moreover, in both the figures, the drop in efficiency can be seen when $0^\circ < \theta < 60^\circ$ for $k_0h > 3.2$. However, with the increase in breakwaters' height, more and more wave energy will be blocked in front of the breakwaters, which in turn leads to a serious decrease in absorption efficiency. The comparison shows that when the rate of absorbed energy increases, the energy conversion efficiency is more. Furthermore, the suitable combination of k_0h and θ, η can enhance the efficiency of the OWC device.

The distribution of OWC efficiency (η) over the range of dimensionless wavenumber (k_0h) and incident wave angle (θ) for different widths of the breakwaters ($b_1/h = b_2/h$) is plotted in Fig. 9. It can be noticed that breakwaters that are wider (Fig. 9(b)) than others, oscillate more frequently than those that are narrower (Fig. 9(a)). Furthermore, it is seen that the efficiency attains the peak multiple times, which may happen due to the sloshing phenomena. Furthermore, it is seen that a reasonable combination of k_0h and θ, η can provide an efficiency (η) of approximately 1. This result indicates that depending on the incident wave angle, an optimized design of the breakwaters results in maximum efficiency in wave power absorption.

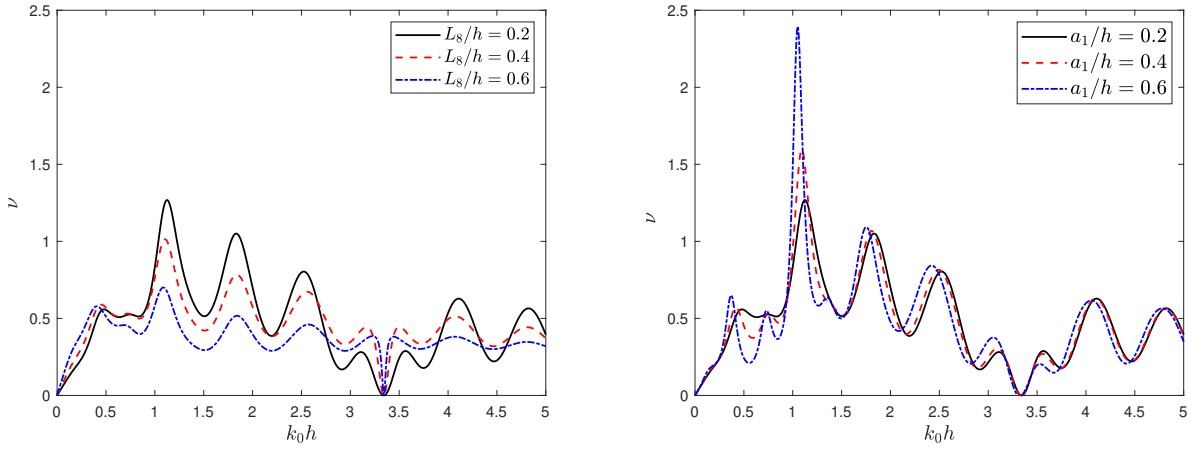

(a) (b)

Figure 10: Radiation conductance of OWC (ν) versus non-dimensional wavenumber (k_0h) for various (a) lengths of the barrier (L_8/h) with $a_1/h = a_2/h = 0.2$, and (b) height of breakwater ($a_1/h = a_2/h$) with $L_8/h = 0.2$. The other fixed parameters are $b_1/h = b_2/h = 1$, $L_{10}/h = 1$, $L_4/h = 5$, $L_2/h = 2$, $L_6/h = 2$ and $\theta = 20^\circ$.

Fig. 10(a) shows an interesting result for radiation conductance of OWC (ν) against non-dimensional wave number (k_0h) for various lengths of the barrier (L_8/h). It is observed that the higher radiation conductance curve appears for a smaller value of L_8/h. Moreover, the radiation conductance increases for $k_0h < 0.5$ and attains a left shifting with an increase in the length of the barrier. Zero radiation conductance of OWC is found when $k_0h \approx 3.4$ for all other wave and structural parameters. Similarly, Fig. 10(b) illustrates the result for radiation conductance of OWC (ν) against non-dimensional wavenumber (k_0h) for various heights of the breakwaters. Observation with care demonstrates that the radiation conductance attains the peak for a larger height of the breakwaters. As seen in Fig. 10(a), here also the radiation conductance is found to be zero when $K_0h \approx 3.4$. The radiation conductance (ν) increases with an increase in height of the breakwater. Therefore, the height of the breakwater

plays a vital role in getting the maximum radiation conductance of the OWC device.

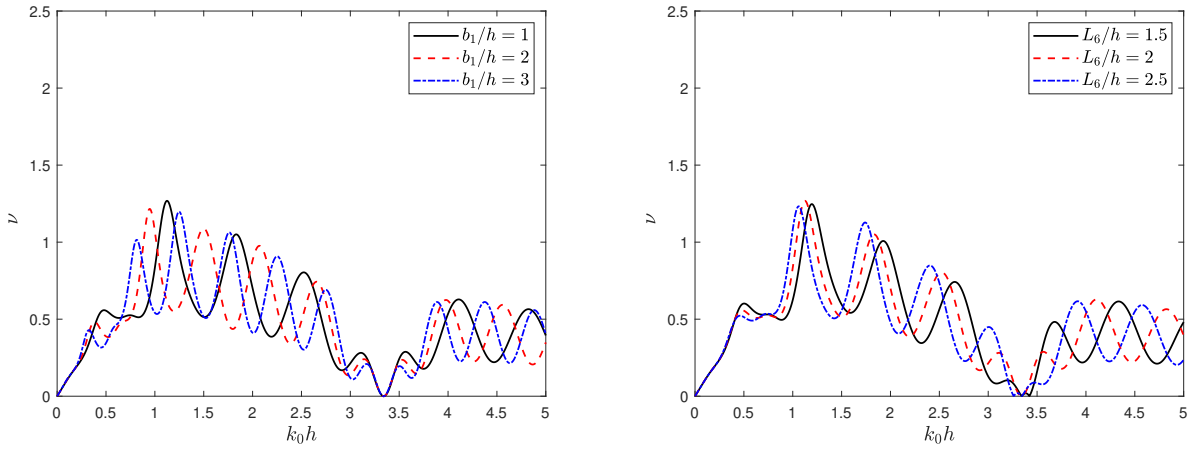

(a) (b)

Figure 11: Radiation conductance of OWC (ν) against non-dimensional wavenumber (k_0h) for various (a) widths of the breakwater ($b_1/h = b_2/h$) with $L_6/h = 2$, and (b) spacing between OWC and rigid structure (L_6/h) with $b_1/h = b_2/h = 1$. The other fixed parameters are $L_8/h = 0.2$, $a_1/h = a_2/h = 0.2$, $L_{10}/h = 1$, $L_4/h = 5$, $L_2/h = 2$, $L_6/h = 2$ and $\theta = 20°$.

Figs. 11(a) and 11(b) show the results for radiation conductance of OWC (ν) against non-dimensional wavenumber (k_0h) for various widths of the breakwaters ($b_1/h = b_2/h$) and spacing between OWC and second breakwater (L_6/h), respectively. From Fig. 11(a), it can be seen that the amplitude of oscillatory curves of radiation conductance decreases with an increase in the width of the breakwaters. Moreover, the maxima of the peak in the resonance occur for lower values of k_0h for all the values of breakwater width. This may happen as the breakwaters' effect on wave propagation takes place with an increase in the widths of the breakwaters. It can be seen that the radiation conductance drops when $k_0h \approx 3.4$. Furthermore, for all the parameters it obeys the oscillating pattern. Similarly, Fig. 11(b) reveals that the radiation conductance of OWC attains a left shifting with increases in spacing between the second breakwater and OWC (L_6/h) for $k_0h < 1.5$. Moreover, for $k_0h < 0.5$, there are no variations found in the radiation conductance curve. Therefore, the width of the breakwater and spacing between the second breakwater and OWC play a vital role in getting the maximum radiation conductance of the OWC device.

Fig. 12(a) dedicates the result for radiation conductance of OWC (ν) against incident wave angle (θ) for various heights of the breakwaters ($a_1/h = a_2/h$). Careful observation reveals that for a smaller height of the breakwaters, the radiation conductance of OWC is more for $\theta < 20°$. The radiation conductance of OWC seems to be zero when $\theta > 85°$. However, a moderate value of the heights of the breakwaters can significantly increase the radiation conductance of the OWC device. Additionally, the peak in the radiation conductance curve can be found for the larger height of the breakwater. Similarly, Fig. 12(b) shows the result for radiation conductance of OWC (ν) against incident wave angle (θ) for different widths of the breakwaters. It can be observed that when the widths of the breakwaters increase, the radiation conductance of OWC decreases for a smaller angle of incidence. A more oscillating pattern in the radiation conductance curve can be seen for the larger

width of the breakwaters. According to preceding Fig. 12(a), zero radiation conductance of OWC is found when $\theta = 90°$. Moreover, the results indicate that, depending upon the incident wave angle, the widths of the breakwaters can be chosen suitably to enhance the radiation conductance of the OWC device.

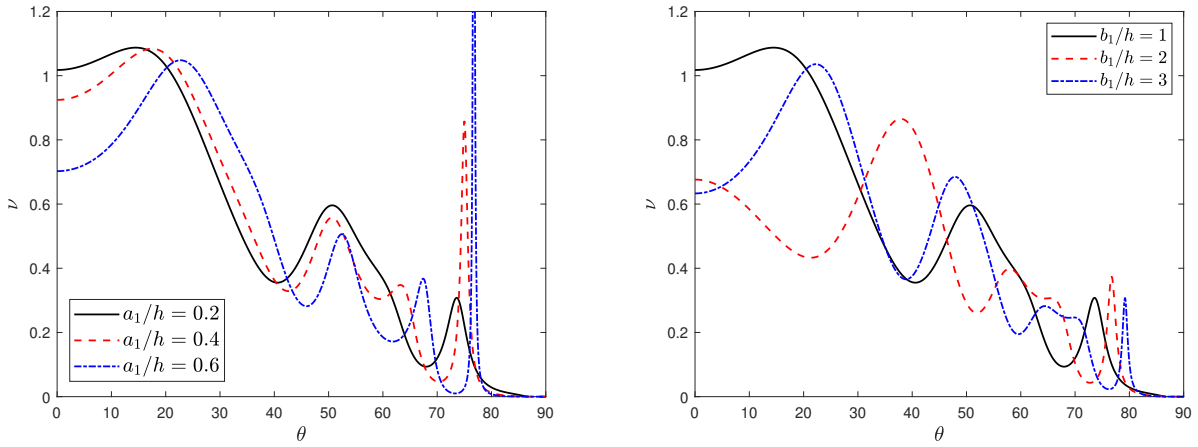

(a) (b)

Figure 12: Radiation conductance of OWC (ν) versus incident wave angle (θ) for various (a) heights of the breakwater ($a_1/h = a_2/h$) with $b_1/h = b_2/h = 1$, and (b) width of the breakwater ($b_1/h = b_2/h$) with $a_1/h = a_2/h = 0.2$. The other fixed parameters are $L_8/h = 0.2$, $L_{10}/h = 1$, $L_4/h = 5$, $L_2/h = 2$, $L_6/h = 2$ and k_0h=1.8.

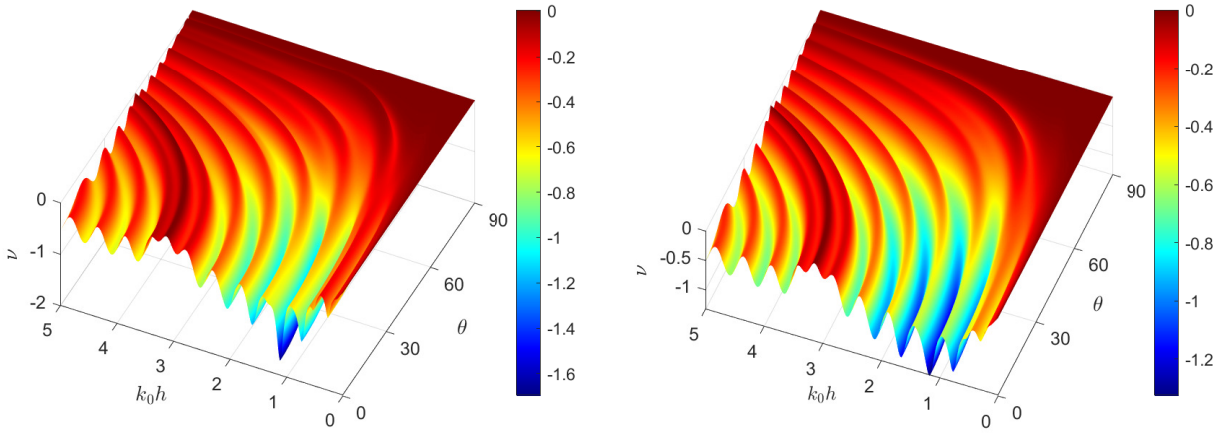

(a) $a_1/h = a_2/h = 0.2$ (b) $a_1/h = a_2/h = 0.4$

Figure 13: Surface plot of radiation conductance of OWC (ν) against non-dimensional wavenumber (k_0h) and different incident wave angle (θ) for various height of the breakwater $a_1/h = a_2/h$. The other fixed parameters are $L_8/h = 0.2$, $b_1/h = b_2/h = 1$, $L_{10}/h = 1$, $L_4/h = 5$, $L_6/h = 2$ and $L_2/h = 2$.

Figs. 13(a) and 13(b) show the surface plot for radiation conductance of OWC (ν) against non-dimensional wavenumber (k_0h) and incident wave angle (θ) for various heights of the breakwaters ($a_1/h = a_2/h$). From both the figures, it is found that the minima in the radiation conductance occur

for $k_0h \approx 1.2$ and $0 < \theta < 60°$. It can be observed that, for less height of the breakwaters, the radiation conductance is more. Moreover, an appropriate combination of k_0h, θ, and ν, along with them all the parameters of breakwaters, can help in increasing the radiation conductance of the OWC device. Furthermore, the observation indicates that depending upon k_0h, a suitable incident wave angle (θ) can be chosen to get optimum radiation conductance of the OWC device.

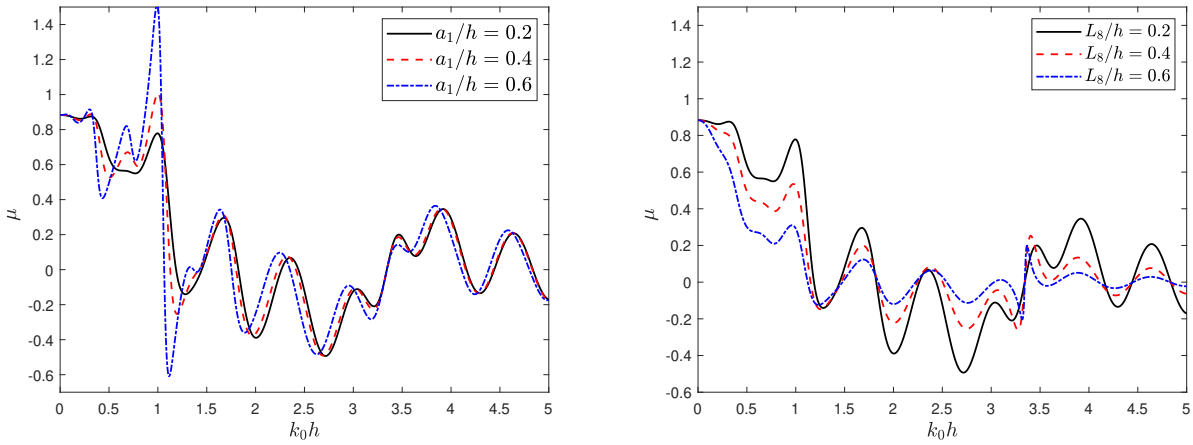

(a) (b)

Figure 14: Radiation susceptance of OWC (μ) versus non-dimensional wavenumber (k_0h) for various (a) heights of the breakwaters ($a_1/h = a_2/h$) with $L_8/h = 0.2$, and (b) length of the barrier (L_8/h) with $a_1/h = a_2/h = 0.2$. The other fixed parameters are $L_6/h = 2$, $b_1/h = b_2/h = 1$, $L_{10}/h = 1$, $L_2/h = 2$, $L_4/h = 5$ and $\theta = 20°$.

Fig. 14(a) shows the result for radiation susceptance of OWC (μ) against non-dimensional wave number (k_0h) for various heights of the breakwaters ($a_1/h = a_2/h$). It is observed that the maxima of the peak in the radiation susceptance of the OWC occur for a larger value of the height of the breakwaters (Fig. 14(a)). This result may occur as the resonance due to the sloshing effect is higher for varying heights of the breakwaters. Similarly, Fig. 14(b) shows the condition for radiation susceptance of OWC (μ) against non-dimensional wave number (k_0h) for different lengths of the barrier (L_8/h). It is evident from the result that the radiation susceptance of OWC decreases with an increase in the length of the barrier in the long wave regime. The oscillatory pattern for radiation susceptance seems more for a smaller barrier.

Fig. 15(a) illustrates the result for radiation susceptance of OWC (μ) against non-dimensional wave number (k_0h) for different widths of the breakwaters ($b_1/h = b_2/h$). It is clear from the result that for $k_0h < 2.6$, the radiation susceptance decreases with an oscillatory pattern and attains the minimum. Furthermore, when the breakwaters' width increases, OWC's radiation susceptance shifts to the left. Similarly, in Fig. 15(b), results for the radiation susceptance of OWC (μ) against non-dimensional wavenumber (k_0h) for different spacing between the second breakwater and OWC (L_6/h) are plotted. Moreover, for $k_0h < 0.5$, there is negligible change in the radiation susceptance curve with an increase in the distance between the second breakwater and the OWC. As the distance between the second breakwater and the OWC increases, the amplitude of the μ curve increases and shifts towards the left. It can be seen that for some wave and structural parameters, the radiation susceptance attains negative

values. It is noteworthy to mention that in the case of radiation susceptance, the improvement is much more in the case of forced oscillation in heave and the pressure-dependent hydrodynamic coefficients.

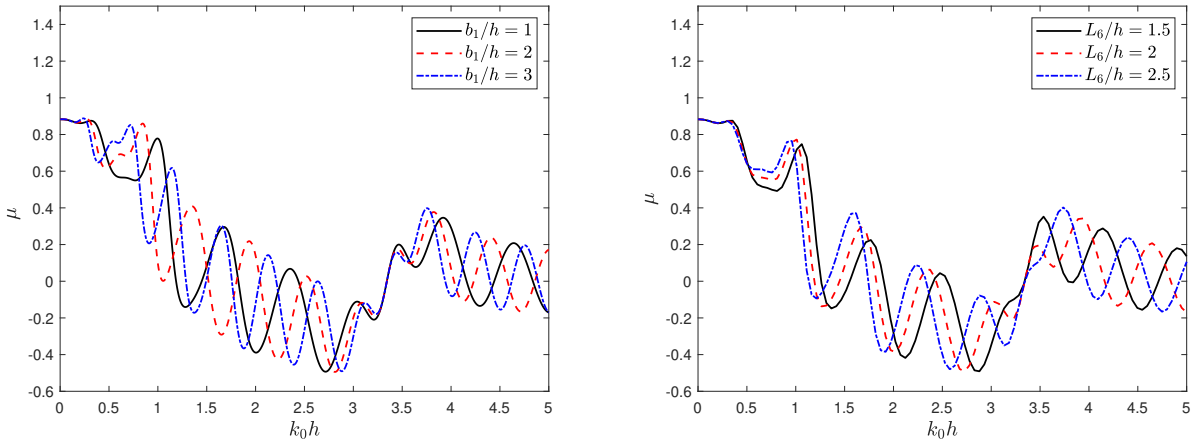

(a) (b)

Figure 15: Radiation susceptance of OWC (μ) versus non-dimensional wavenumber (k_0h) for various (a) width of breakwater ($b_1/h = b_2/h$) with $L_6/h = 2$, and (b) spacing between second breakwater and barrier (L_6/h) with $b_1/h = b_2/h = 1$. The other fixed parameters are $L_8/h = 0.2$, $a_1/h = a_2/h = 0.2$, $L_{10}/h = 1$, $L_4/h = 5$, $L_2/h = 2$ and $\theta = 20°$.

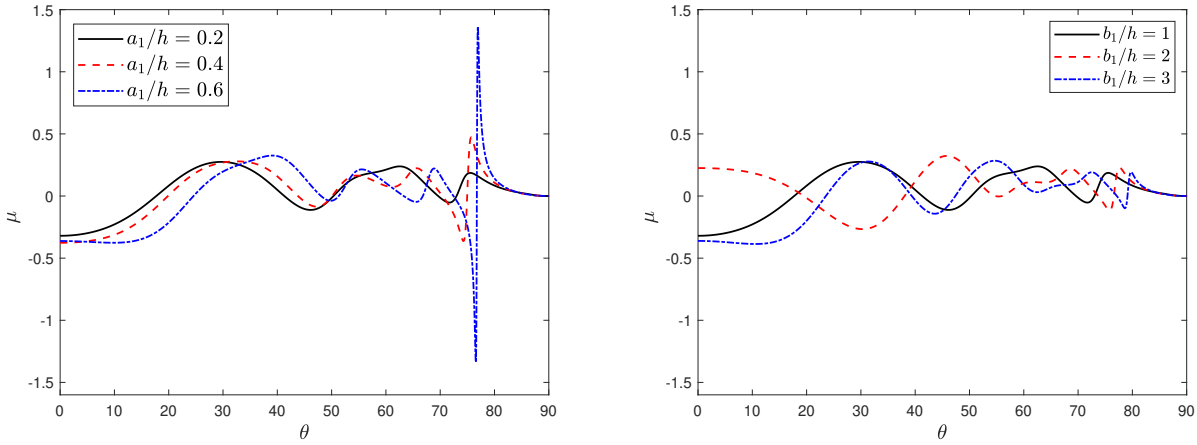

(a) (b)

Figure 16: Radiation susceptance of OWC (μ) versus incident wave angle (θ) for various (a) heights of the breakwater ($a_1/h = a_2/h$) with $b_1/h = b_2/h = 1$, and (b) width of the breakwaters ($b_1/h = b_2/h$) with $a_1/h = a_2/h = 0.2$. The other fixed parameters are $L_8/h = 0.2$, $L_{10}/h = 1$, $L_4/h = 5$, $L_2/h = 2$, $L_6/h = 2$ and k_0h=1.8.

Fig. 16(a) illustrates the result for radiation susceptance of OWC (μ) against incident wave angle (θ) for different heights of the breakwaters ($a_1/h = a_2/h$). It can be noticed that the radiation susceptance of OWC decreases with an increase in the height of the breakwaters for $\theta < 30°$. Moreover, the highest peak for radiation susceptance is found for a higher value of the height of the breakwaters. Furthermore, the radiation susceptance of OWC attains the optima at $\theta \approx 78°$ for $a_1/h = 0.6$ with

some of the physical parameters. Similarly, Fig.16(b) shows the radiation susceptance of the OWC concerning incident wave angle (θ) for different widths of the breakwaters. It can be concluded that irrespective of the breakwaters' width, the amplitude of the oscillatory pattern of radiation susceptances decreases with an increase in the value of θ and diminishes when $80^\circ < \theta < 90^\circ$.

5.3. Effects of double trenches

Fig. 17(a) presents the result for maximum efficiency of OWC (η) against non-dimensional wavenumber (k_0h) for three different cases like the absence of trench and the presence of single and double trenches. The patterns of the efficiency curves and observations are similar to that observed in the presence of single and double breakwaters as discussed in the previous section. The figures show that more oscillating patterns in the efficiency curve of OWC can be found in the presence of double trenches as compared to a single one. When $k_0h \approx 3.4$, zero efficiencies of OWC are found in all these three cases. Similarly, Fig. 17(b) depicts the result for maximum efficiency of OWC (η) against dimensionless wave number (k_0h) for various depths of trenches ($a_1/h = a_2/h$). The panel reveals that for smaller and larger k_0h, there are negligible changes in the efficiency curve with an increase in the depth of the trenches. The amplitude of the oscillatory pattern increases with an increase in the depth of the trenches for intermediate values of k_0h. A similar observation was found in the presence of double breakwaters as shown in Fig. 4(b).

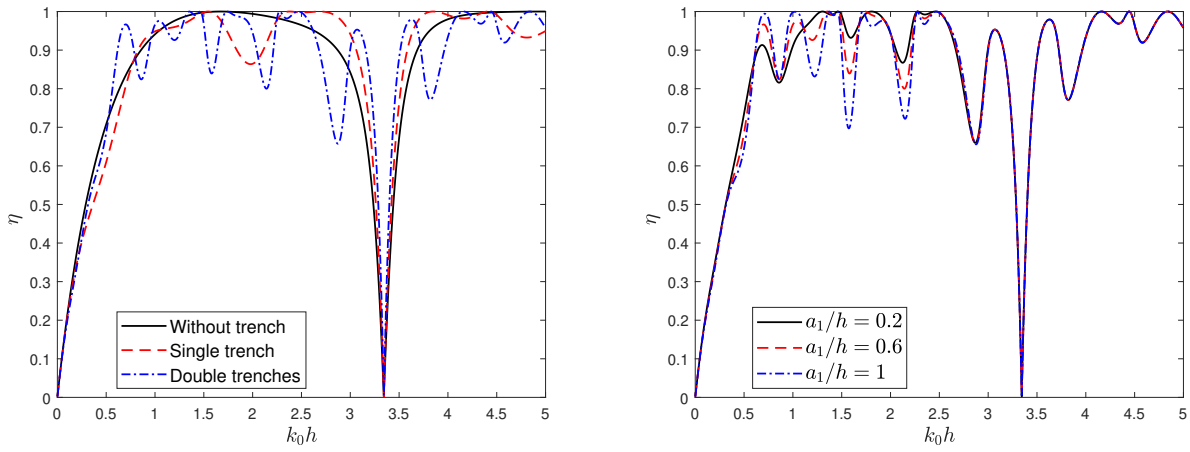

(a) (b)

Figure 17: Maximum efficiency of OWC (η) versus non-dimensional wavenumber (k_0h) (a) in the absence of trench ($a_1/h = a_2/h \to 0$), presence of single trench ($a_1/h = 1, a_2/h = 0$), double trenches($a_1/h = a_2/h = 1$) for different cases with $L_6/h = 2$, and (b) for various $a_1/h = a_2/h$ with $b_1/h = b_2/h = 1$. The other fixed parameters are $L_8/h = 0.2$, $L_{10}/h = 1$, $L_4/h = 5$, $L_2/h = 2$, $L_6/h = 2$ and $\theta = 20^\circ$.

Fig. 18(a) demonstrates the results for maximum efficiency of OWC (η) against non-dimensional wavenumber (k_0h) for various widths of the trenches($b_1/h = b_2/h$). It can be seen that OWC efficiency is significantly affected by the wider widths of the trenches. For smaller $k_0h < 0.8$, there is no change in the efficiency for changing the width of the trenches. Moreover, the minima of the efficiency curves follow a left-shifting behavior with an increase in the width of the trenches. Furthermore, the

oscillatory pattern seems more for a larger width of the breakwaters. Fig. 18(b) displays the result for OWC efficiency against non-dimensional wave number (k_0h) for different barrier lengths. The observation discloses that with an increase in barrier length, the efficiency rises. Furthermore, it is observed that the efficiency of OWC attains zero when $k_0h \approx 3.4$.

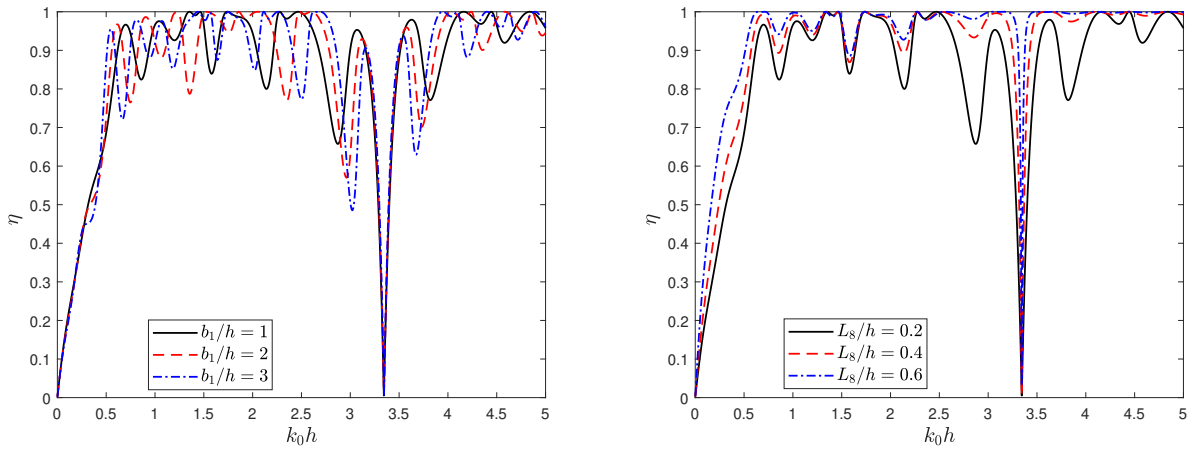

(a) (b)

Figure 18: Maximum efficiency of OWC (η) versus non-dimensional wavenumber (k_0h) for various (a) width of trenches ($b_1/h = b_2/h$) with $L_8/h = 0.2$, and (b) length of barrier (L_8/h) with $b_1/h = b_2/h = 1$. The other fixed parameters are $a_1/h = a_2/h = 0.6$, $L_6/h = 2$, $L_{10}/h = 1$, $L_4/h = 5$, $L_2/h = 2$ and $\theta = 20°$.

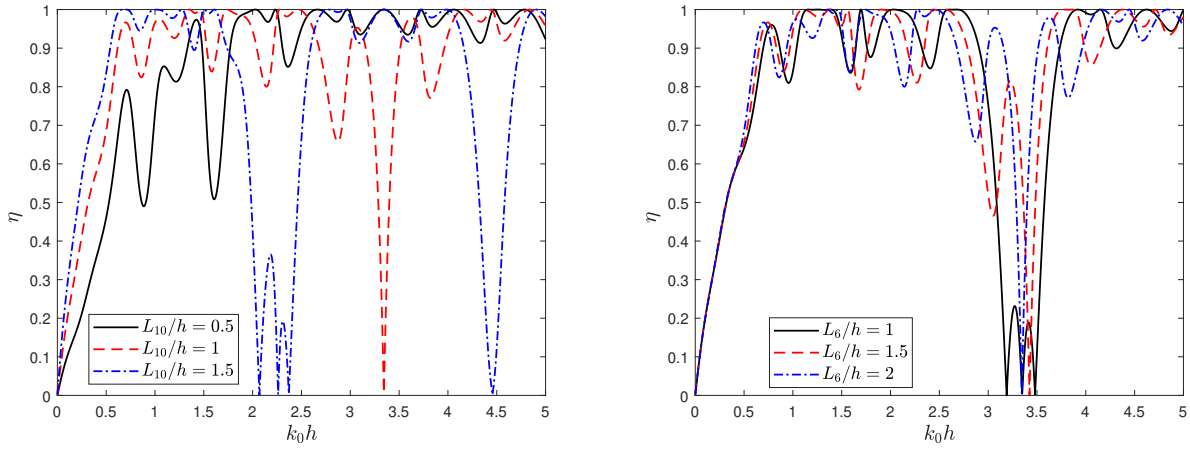

(a) (b)

Figure 19: Maximum efficiency of OWC (η) versus non-dimensional wavenumber k_0h for various (a) spacing between OWC to the rigid wall (L_{10}/h) with $L_6/h = 2$, and (b) spacing between the second trench and OWC (L_6/h) with $L_{10}/h = 1$. The other fixed parameters are $L_8/h = 0.2$, $L_4/h = 5$, $a_1/h = a_2/h = 0.6$, $b_1/h = b_2/h = 1$, $L_2/h = 2$ and $\theta = 20°$.

Fig. 19(a) illustrates the results for maximum efficiency of OWC (η) against non-dimensional wavenumber (k_0h) for various spacing between OWC and rigid wall (L_{10}/h). This figure reveals that the efficiency curve of OWC (η) increases as the spacing between OWC and rigid wall increases

for the long-wave region. Moreover, zero efficiencies are observed multiple times for wider L_{10}/h. In addition, subharmonic peaks in the efficiency curve are observed. With a rise in k_0h, efficiency increases exponentially for lower L_{10}/h, yielding multiple times full efficiency. Furthermore, the oscillatory pattern diminishes in the short-wave region. Fig. 19(b) shows the result for maximum efficiency of OWC (η) against non-dimensional wavenumber (k_0h) for various spacing between the second trench and OWC (L_6/h). This figure shows that no changes in the efficiency curve are found for $k_0h < 0.5$. Moreover, multiple times zero efficiencies are observed for smaller L_6/h. The amplitude of the efficiency curves seems to be increasing with a left-shifting pattern for increasing the spacing between the second trench and OWC.

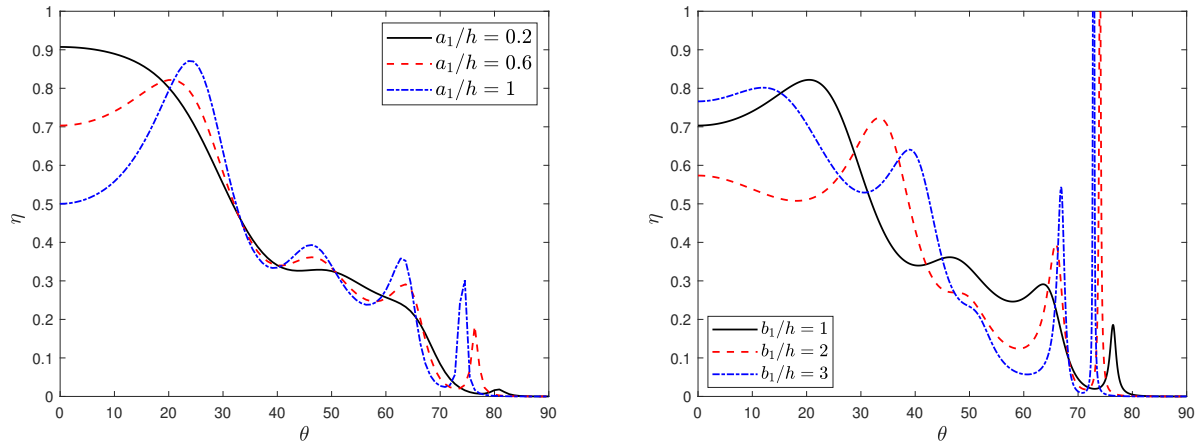

(a) (b)

Figure 20: Maximum efficiency of OWC (η) versus θ for various (a) depth of the trenches ($a_1/h = a_2/h$) with $b_1/h = b_2/h = 1$, and (b) width of the trenches ($b_1/h = b_2/h$) with $a_1/h = a_2/h = 0.6$. The other fixed parameters are $L_8/h = 0.2$, $L_4/h = 5$, $L_2/h = 2$, $L_6/h = 2$, $L_{10}/h = 1$ and $k_0h = 1$.

Fig. 20(a) illustrates the results for maximum efficiency of OWC (η) against θ for various depths of the trenches ($a_1/h = a_2/h$). It is observed that the efficiency is more for smaller depths ($a_1/h = a_2/h$) of trenches for $\theta < 30°$. The efficiency decreases in an oscillatory pattern for increasing the incidence angle. Zero efficiencies of OWC can be found when $\theta > 80°$. A more oscillating pattern of the efficiency curve is found for a larger depth of the trenches. Fig. 20 (b) exhibits the variation for maximum efficiency of OWC (η) against incident wave angle (θ) for various widths of the trenches. It can be seen that full efficiency is found for the larger width of the trenches for $70° < \theta < 80°$. Furthermore, trenches having larger widths have a more oscillating pattern. Zero efficiencies of OWC can be observed when $\theta > 80°$ as described in Fig. 20(a) as observed in Fig. 20(a).

The results for the radiation susceptance of OWC (μ) versus non-dimensional (k_0h) for different trenches depths ($a_1/h = a_2/h$) are shown in Fig. 21(a). The peak in radiation susceptance is found for the larger depth of the trenches. For $k_0h > 2.5$, the radiation susceptance curves remain unchanged for all the parameters of the depth of the trench. The radiation susceptance increases with an increase in the depth of the trenches for k_0h at 1.5. Moreover, the oscillatory pattern is more for the larger depth of the trenches. Further, the drop in the radiation susceptance curve is observed for the larger

depth of the trench. The results for the radiation susceptance of OWC (μ) against non-dimensional wavenumber (k_0h) for different widths of the trenches are shown in Fig. 21(b). It is found from the result that, the peak in the radiation susceptance curve occurs for larger width of trenches. The radiation susceptance curve increases with an increase in the width of the trenches and attains a left shifting for the smaller k_0h.

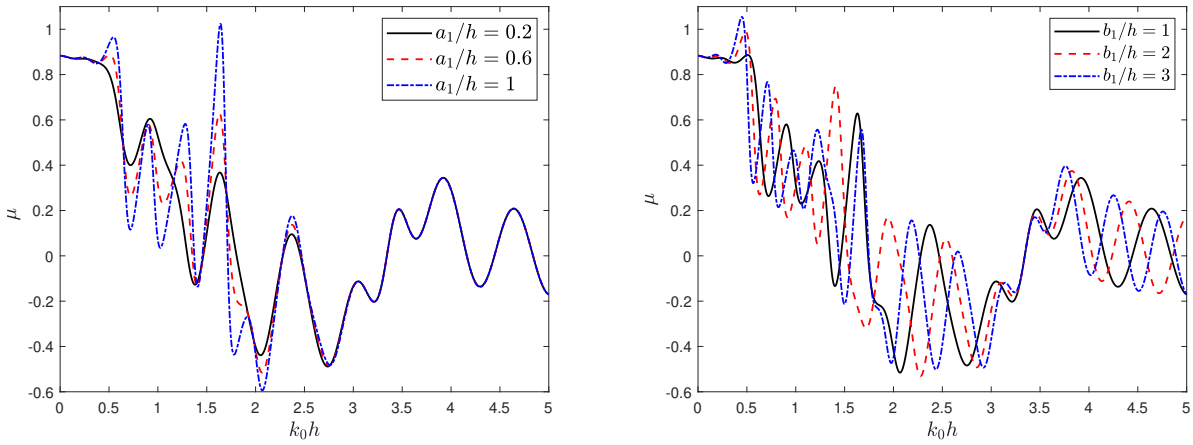

(a) (b)

Figure 21: Radiation susceptance of OWC (μ) versus k_0h for various (a) depth of the trenches ($a_1/h = a_2/h$) with $b_1/h = b_2/h = 1$, and (b) width of the trenches ($b_1/h = b_2/h$) with $a_1/h = a_2/h = 0.6$. The other fixed parameters are $L_8/h = 0.2$, $L_4/h = 5$, $L_6/h = 2$, $L_2/h = 2$, $L_{10}/h = 1$ and $\theta = 20°$.

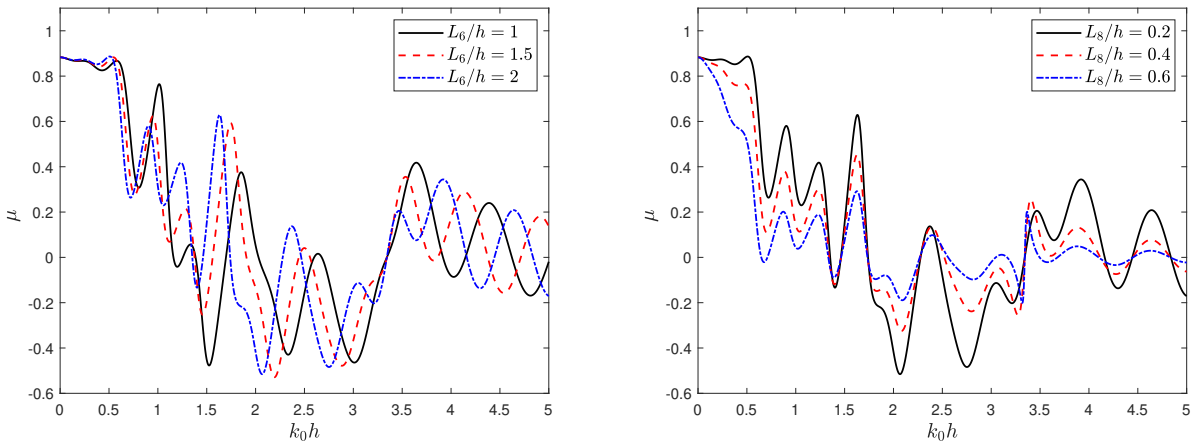

(a) (b)

Figure 22: Radiation susceptance of OWC (μ) versus k_0h for various (a) spacing between trench to OWC (L_6/h) with $L_8/h = 0.2$, and (b) lengths of the barrier (L_8/h) with $L_6/h = 2$. The other fixed parameters are $a_1/h = a_2/h = 0.6$, $b_1/h = b_2/h = 1$, $L_2/h = 2$, $L_4/h = 5$, $L_{10}/h = 1$ and $\theta = 20°$.

Fig. 22(a) illustrates the results for radiation susceptance of OWC (μ) against non-dimensional wavenumber (k_0h) for various spacing between the second trench and OWC (L_6/h). In general, the

radiation susceptance curve is more oscillatory with an increase in (L_6/h) with a left shift. However, there is a negligible change in the radiation susceptance curve for smaller k_0h. Fig. 22(b), describes the result for radiation susceptance of OWC (μ) against non-dimensional wavenumber (k_0h) for various lengths of the barrier (L_8/h). It is observed that the radiation susceptance curve decreases with an increase in the length of the barrier for $k_0h < 1.5$. The drop in radiation susceptance of OWC is found for smaller L_8/h. Further, in comparison to smaller barrier lengths, larger barrier lengths depict a more oscillatory pattern.

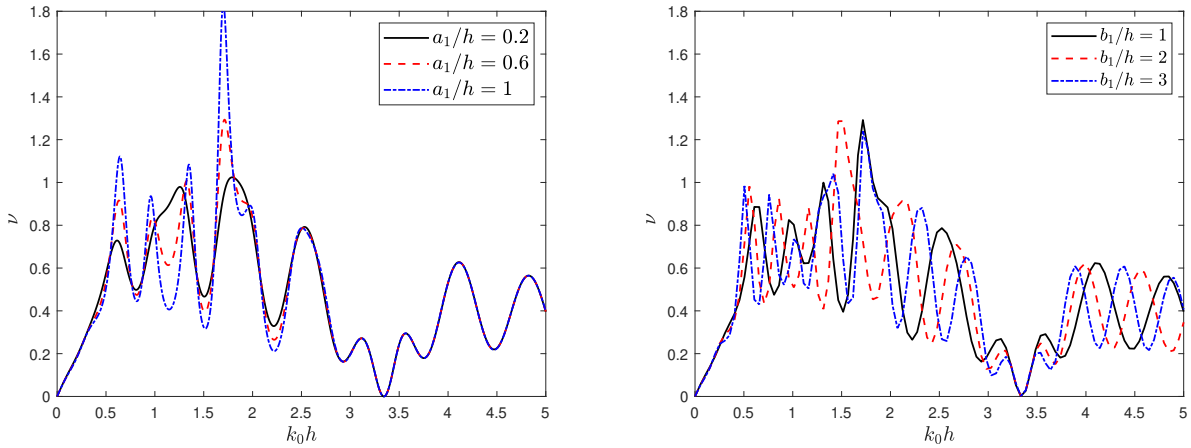

(a) (b)

Figure 23: Radiation conductance of OWC (ν) versus k_0h for various (a) depth of the trenches ($a_1/h = a_2/h$) with $b_1/h = b_2/h = 1$, and (b) widths of the trenches ($b_1/h = b_2/h$) with $a_1/h = a_2/h = 0.6$. The other fixed parameters are $L_8/h = 0.2$, $L_6/h = 2$, $L_2/h = 2$, $L_4/h = 5$, $L_{10}/h = 1$ and $\theta = 20°$.

Fig. 23(a) depicts the results for radiation conductance of OWC (ν) against non-dimensional wavenumber (k_0h) for various depths of the trenches($a_1/h = a_2/h$). It is found that higher OWC radiation conductivity is found for larger depths of the trenches. Moreover, the peak in the radiation conductance curve occurs for the higher depths of trenches. Zero radiation conductance occurs for $k_0h = 3.4$. The amplitude of the radiation conductance curve increases with an increase in the depth of the trenches for $0.5 < k_0h < 2.5$. However, no changes in the radiation susceptance curve are observed for $k_0h > 2.5$ for all other structural parameters. Fig. 23(b), shows the result for radiation conductance of OWC (ν) against the non-dimensional wave number (k_0h) for various widths of the trenches. It is observed that the radiation conductance curve is more oscillatory for a larger width of the trenches.

Fig. 24(a) shows the results for radiation conductance of OWC (ν) against non-dimensional wavenumber (k_0h) for various lengths of the barrier. The higher radiation conductance is found for the shorter length of the barrier. The radiation conductance attains a left shifting with an increase in the length of the barrier. As shown in the previous figures, in this case also zero radiation conductance is found at $k_0h = 3.4$. Fig. 24(b) shows the result for radiation conductance of OWC (ν) against non-dimensional wave number (k_0h) for various spacing between the second trench and OWC. The figure depicts that in the short wave region, the amplitude of the radiation conductance curves increases

with a left-shifting for an increase in the spacing between the second trench and OWC. Moreover, zero radiation conductance is found for $3 < k_0h < 3.5$.

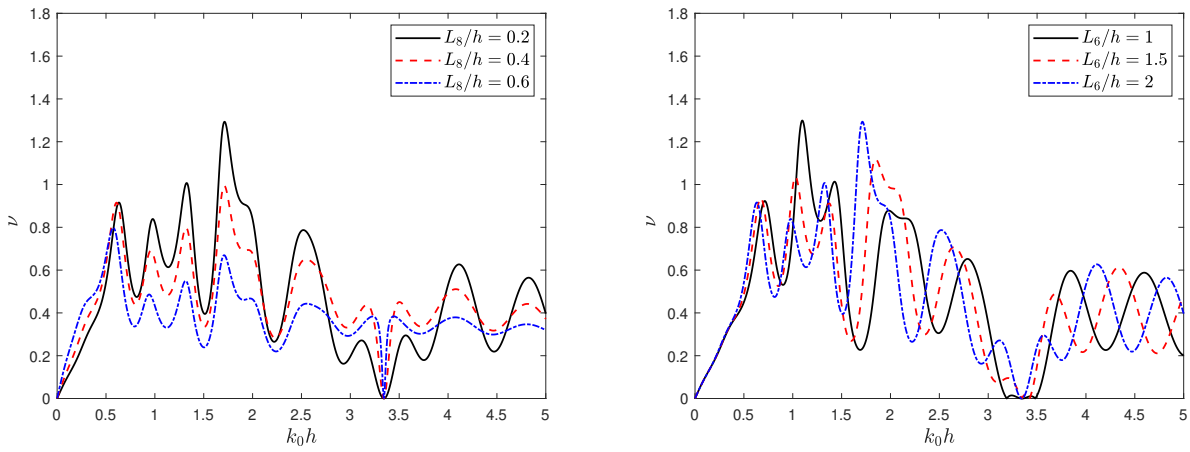

(a) (b)

Figure 24: Radiation conductance of OWC (ν) versus k_0h for various (a) lengths of the barrier (L_8/h) with $L_6/h = 2$, and (b) spacing between the trench and OWC (L_6/h) with $L_8/h = 0.2$. The other fixed parameters are $a_1/h = a_2/h = 0.6$, $b_1/h = b_2/h = 1$, $L_{10}/h = 1$, $L_4/h = 5$, $L_2/h = 2$ and $\theta = 20°$.

6. Conclusions

The impact of trenches and submerged breakwaters on the effectiveness of the OWC device is analyzed in this study. The associated boundary value is solved by coupling the eigenfunction expansion, and multi-domain boundary element approaches. A simplified expression for the efficiency, along with all the coefficients of the OWC device, is acknowledged. There is good agreement between the earlier and current results when they are compared as a specific case. The study reveals that the efficiency and other hydrodynamic performances of the OWC device are significantly impacted by the height of breakwaters and the depth of trenches. However, OWC's effectiveness has negligible effect as breakwaters widths increase. Moreover, almost zero efficiencies happen and exhibit a shift to the left as the spacing between the second breakwater and OWC rises. At larger OWC width, zero efficiencies are observed more frequently. Efficiency grows exponentially with an oscillatory pattern with an increase in k_0h for a smaller width of the OWC and results in multiple times full efficiency. The efficiency curve of OWC shows an oscillating pattern due to the presence of submerged breakwaters and trenches. In the case of flat bottom, in a specific range of k_0h, one-time full efficiency was observed; however, the presence of breakwaters/trenches resulted in multiple times full efficiency. In comparison to a single one, the twin breakwaters and trenches have a higher impact on the efficiency of OWC. For both the cases of breakwaters and trenches, zero efficiencies of OWC are found when $k_0h = 3.4$. To perform more accurate system behavior prediction, these above impacts must be taken into account. It is, in general, observed that the efficiency of the OWC device is always maximum, which enhances the performance of the OWC device unless some kind of breakwaters or trenches is

placed. Hence, the efficiency of the OWC device is probably affected unless breakwaters and trenches are placed along with it. In conclusion, placing submerged breakwaters and trenches with an OWC device can significantly alter the device's performance over the wide frequency range.

Acknowledgment: HB gratefully acknowledges the financial support from the Science and Engineering Research Board, Dept. of Science and Technology, Govt. of India, through the MATRICS project (Award Number MTR/2021/000870). SZ acknowledges support from the Open Research Fund Program of the State Key Laboratory of Hydraulic Engineering Simulation and Safety (Tianjin University) [Grant No. HESS-1902].

Declaration of interests: The authors report no conflict of interest.

Data Availability: The data that supports the findings of this study are available within the article, highlighted in each of the figure captions and corresponding discussions.

References

Emre Ozkop and Ismail H Altas. Control, power and electrical components in wave energy conversion systems: A review of the technologies. *Renewable and Sustainable Energy Reviews*, 67:106–115, 2017.

Jie Liu, Yuchen Zhang, Kai Zhang, Jianzhong Fan, Chuan-Kui Wang, and Lili Lin. Bicolor switching mechanism of multifunctional light-emitting molecular material in solid phase. *Organic Electronics*, 71:212–219, 2019.

Godfrey Boyle. *Renewable energy: power for a sustainable future*, volume 2. Oxford University Press, 2004.

K Rezanejad, J Bhattacharjee, and C Guedes Soares. Stepped sea bottom effects on the efficiency of nearshore oscillating water column device. *Ocean Engineering*, 70:25–38, 2013.

TV Heath. A review of oscillating water columns. *Philosophical Transactions of the Royal Society A: Mathematical, Physical and Engineering Sciences*, 370(1959):235–245, 2012.

Johannes Falnes. A review of wave-energy extraction. *Marine Structures*, 20(4):185–201, 2007.

F de O Antonio. Wave energy utilization: A review of the technologies. *Renewable and Sustainable Energy Reviews*, 14 (3):899–918, 2010.

DV Evans and R Porter. Hydrodynamic characteristics of an oscillating water column device. *Applied Ocean Research*, 17(3):155–164, 1995.

Utku Şentürk and Aydoğan Özdamar. Modelling the interaction between water waves and the oscillating water column wave energy device. *Mathematical and Computational Applications*, 16(3):630–640, 2011.

Nicola Delmonte, Davide Barater, Francesco Giuliani, Paolo Cova, and Giampaolo Buticchi. Oscillating water column power conversion: A technology review. In *2014 IEEE Energy Conversion Congress and Exposition (ECCE)*, pages 1852–1859. IEEE, 2014.

De-Zhi Ning, Jin Shi, Qing-Ping Zou, and Bin Teng. Investigation of hydrodynamic performance of an OWC (oscillating water column) wave energy device using a fully nonlinear HOBEM (higher-order boundary element method). *Energy*, 83:177–188, 2015.

Chen Wang and Yongliang Zhang. Hydrodynamic performance of an offshore oscillating water column device mounted over an immersed horizontal plate: A numerical study. *Energy*, 222:119964, 2021.

LMC Gato, V Warfield, and A Thakker. Performance of a high-solidity wells turbine for an OWC wave power plant. *Journal of Energy Resources Technology*, 118(4):263–268, 1996.

A Brito-Melo, LMC Gato, and AJNA Sarmento. Analysis of Wells turbine design parameters by numerical simulation of the OWC performance. *Ocean Engineering*, 29(12):1463–1477, 2002.

YMC Delauré and A Lewis. 3D hydrodynamic modelling of fixed oscillating water column wave power plant by a boundary element methods. *Ocean Engineering*, 30(3):309–330, 2003.

María L Jalón and Feargal Brennan. Hydrodynamic efficiency versus structural longevity of a fixed OWC wave energy converter. *Ocean Engineering*, 206:107260, 2020.

Mohamin BM Khan and Harekrushna Behera. Impact of sloping porous seabed on the efficiency of an OWC against oblique waves. *Renewable Energy*, 173:1027–1039, 2021.

Lin Cui, Siming Zheng, Yongliang Zhang, Jon Miles, and Gregorio Iglesias. Wave power extraction from a hybrid oscillating water column-oscillating buoy wave energy converter. *Renewable and Sustainable Energy Reviews*, 135: 110234, 2021.

Rongquan Wang, Dezhi Ning, and Chongwei Zhang. Numerical investigation of the hydrodynamic performance of the dual-chamber oscillating water columns. In *The 27th International Ocean and Polar Engineering Conference*. OnePetro, 2017.

Dezhi Ning, Yu Zhou, and Chongwei Zhang. Hydrodynamic modeling of a novel dual-chamber OWC wave energy converter. *Applied Ocean Research*, 78:180–191, 2018.

De-zhi Ning, Rong-quan Wang, Li-fen Chen, and Ke Sun. Experimental investigation of a land-based dual-chamber OWC wave energy converter. *Renewable and Sustainable Energy Reviews*, 105:48–60, 2019.

Ali Taherian Haghighi, Amir H Nikseresht, and Mohammad Hayati. Numerical analysis of hydrodynamic performance of a dual-chamber oscillating water column. *Energy*, 221:119892, 2021.

Yongyao Luo, Jean-Roch Nader, Paul Cooper, and Song-Ping Zhu. Nonlinear 2d analysis of the efficiency of fixed oscillating water column wave energy converters. *Renewable Energy*, 64:255–265, 2014.

Chen Wang, Yongliang Zhang, and Zhengzhi Deng. Theoretical analysis on hydrodynamic performance for a dual-chamber oscillating water column device with a pitching front lip-wall. *Energy*, 226:120326, 2021.

Chen Wang and Yongliang Zhang. Performance enhancement for a dual-chamber OWC conceived from side wall effects in narrow flumes. *Ocean Engineering*, 247:110552, 2022.

Yu Zhou, Dezhi Ning, and Rongquan Wang. Experimental study on a 3D offshore-stationary dual-chamber OWC wave energy converter. In *The 29th International Ocean and Polar Engineering Conference*. OnePetro, 2019.

Siming Zheng, Alessandro Antonini, Yongliang Zhang, Deborah Greaves, Jon Miles, and Gregorio Iglesias. Wave power extraction from multiple oscillating water columns along a straight coast. *Journal of Fluid Mechanics*, 878:445–480, 2019.

Damon Howe, Jean-Roch Nader, and Gregor Macfarlane. Performance analysis of a floating breakwater integrated with multiple oscillating water column wave energy converters in regular and irregular seas. *Applied Ocean Research*, 99: 102147, 2020.

Jeong-Seok Kim and Bo Woo Nam. Numerical analysis for hydrodynamic performance of OWC devices with multiple chambers in waves. *Journal of Ocean Engineering and Technology*, 36(1):21–31, 2022.

David G Dorrell, Min-Fu Hsieh, and Chi-Chien Lin. A multichamber oscillating water column using cascaded savonius turbines. *IEEE Transactions on Industry Applications*, 46(6):2372–2380, 2010.

Mohammad Shalby, Paul Walker, and David G Dorrell. The investigation of a segment multi-chamber oscillating water column in physical scale model. In *2016 IEEE International Conference on Renewable Energy Research and Applications (ICRERA)*, pages 183–188. IEEE, 2016.

Kourosh Rezanejad, Joydip Bhattacharjee, and Carlos Guedes Soares. Analytical and numerical study of nearshore multiple oscillating water columns. *Journal of Offshore Mechanics and Arctic Engineering*, 138(2), 2016.

Siming Zheng, Alessandro Antonini, Yongliang Zhang, Jon Miles, Deborah Greaves, Guixun Zhu, and Gregorio Iglesias. Hydrodynamic performance of a multi-oscillating water column (OWC) platform. *Applied Ocean Research*, 99: 102168, 2020.

Francis CK Ting and Fredric Raichlen. Wave interaction with a rectangular trench. *Journal of Waterway, Port, Coastal, and Ocean Engineering*, 112(3):454–460, 1986.

P Kar, T Sahoo, and H Behera. Effect of bragg scattering due to bottom undulation on a floating dock. *Wave Motion*, 90: 121–138, 2019.

J Gao, X Ma, G Dong, H Chen, Q Liu, and J Zang. Investigation on the effects of Bragg reflection on harbor oscillations.

Coastal Engineering, 170:103977, 2021.

P Kar, S Koley, and T Sahoo. Scattering of surface gravity waves over a pair of trenches. *Applied Mathematical Modelling*, 62:303–320, 2018.

P Kar, S Koley, and T Sahoo. Bragg scattering of long waves by an array of trenches. *Ocean Engineering*, 198:107004, 2020.

Cynthia D Wang and Michael H Meylan. The linear wave response of a floating thin plate on water of variable depth. *Applied Ocean Research*, 24(3):163–174, 2002.

Gregory S Payne, Jamie RM Taylor, Tom Bruce, and Penny Parkin. Assessment of boundary-element method for modelling a free-floating sloped wave energy device. part 1: Numerical modelling. *Ocean Engineering*, 35(3-4):333–341, 2008.

Ching-Yun Yueh and Shih-Hsuan Chuang. A boundary element model for a partially piston-type porous wave energy converter in gravity waves. *Engineering Analysis with Boundary Elements*, 36(5):658–664, 2012.

Michael H Meylan and Colm J Fitzgerald. The singularity expansion method and near-trapping of linear water waves. *Journal of Fluid Mechanics*, 755:230–250, 2014.

Michael H Meylan, Luke G Bennetts, and Malte A Peter. Water-wave scattering and energy dissipation by a floating porous elastic plate in three dimensions. *Wave Motion*, 70:240–250, 2017.

Mohamin BM Khan and Harekrushna Behera. Analysis of wave action through multiple submerged porous structures. *Journal of Offshore Mechanics and Arctic Engineering*, 142(1):011101, 2020.

KG Vijay, S Neelamani, T Sahoo, K Al-Salem, and CS Nishad. Scattering of gravity waves by a pontoon type breakwater with a series of pervious and impervious skirt walls. *Ships and Offshore Structures*, 17(1):130–142, 2022.

J Mackerle and T Andersson. Boundary element software in engineering. *Advances in Engineering Software (1978)*, 6 (2):66–102, 1984.

Louis Papillon, Ronan Costello, and John V Ringwood. Boundary element and integral methods in potential flow theory: A review with a focus on wave energy applications. *Journal of Ocean Engineering and Marine Energy*, 6:303–337, 2020.

Yingyi Liu, Ying Gou, Bin Teng, and Shigeo Yoshida. An extremely efficient boundary element method for wave interaction with long cylindrical structures based on free-surface Green's function. *Computation*, 4(3):36, 2016.

Mohamin BM Khan, Harekrushna Behera, Trilochan Sahoo, and S Neelamani. Boundary element method for wave trapping by a multi-layered trapezoidal breakwater near a sloping rigid wall. *Meccanica*, 56:317–334, 2021.

Kshma Trivedi and Santanu Koley. Mathematical modeling of breakwater-integrated oscillating water column wave energy converter devices under irregular incident waves. *Renewable Energy*, 178:403–419, 2021.

John L Hess and A_M O Smith. Calculation of potential flow about arbitrary bodies. *Progress in Aerospace Sciences*, 8: 1–138, 1967.

John L Hess. Higher order numerical solution of the integral equation for the two-dimensional neumann problem. *Computer Methods in Applied Mechanics and Engineering*, 2(1):1–15, 1973.

Sewan Park, Kyong-Hwan Kim, Bo Woo Nam, Jeong-Seok Kim, and Keyyong Hong. A study on effects of breakwater on performance of OWC. In *The Thirteenth ISOPE Pacific/Asia Offshore Mechanics Symposium*. OnePetro, 2018.

Zhengzhi Deng, Zhenhua Huang, and Adrian WK Law. Wave power extraction from a bottom-mounted oscillating water column converter with a V-shaped channel. *Proceedings of the Royal Society A: Mathematical, Physical and Engineering Sciences*, 470(2167):20140074, 2014.

Sewan Park, Kyong-Hwan Kim, Bo-Woo Nam, Jeong-Seok Kim, and Keyyong Hong. Experimental and numerical analysis of performance of oscillating water column wave energy converter applicable to breakwaters. In *International Conference on Offshore Mechanics and Arctic Engineering*, volume 58899, page V010T09A044. American Society of Mechanical Engineers, 2019.

Zhengzhi Deng, Lin Wang, Xizeng Zhao, and Peng Wang. Wave power extraction by a nearshore oscillating water column converter with a surging lip-wall. *Renewable Energy*, 146:662–674, 2020.

Zhengzhi Deng, Pinjie Wang, and Pengda Cheng. Hydrodynamic performance of an asymmetry OWC device mounted on a box-type breakwater. *Frontiers in Marine Science*, 8:677030, 2021.

Robert G Dean and Robert A Dalrymple. *Water wave mechanics for engineers and scientists*, volume 2. World Scientific,

1991.

R Gayathri, Mohamin BM Khan, and Harekrushna Behera. Attenuation of wave force on a floating dock by multiple porous breakwaters. *Engineering Analysis with Boundary Elements*, 143:170–189, 2022.

Kourosh Rezanejad, Joydip Bhattacharjee, and C Guedes Soares. Analytical and numerical study of dual-chamber oscillating water columns on stepped bottom. *Renewable Energy*, 75:272–282, 2015.